A new dataset of rain cells ~~generated from~~based on observations of ~~the~~ Tropical Rainfall Measuring Mission (TRMM) precipitation radar ~~and~~, visible ~~and~~ /infrared scanner and microwave imager

Zhenhao Wu[1], ~~Yunfei Fu[1]~~Jian Shang[2], Chunguan Cui[3], Peng Zhang[2], Songyan Gu[2], and Lin Chen[2]~~——~~, Yunfei Fu[1]

[1]School of Earth and Space Sciences, CMA-USTC Laboratory of Fengyun Remote Sensing, University of Science and Technology of China, Hefei, 230026, China

[2]Key Laboratory of Radiometric Calibration and Validation for Environmental Satellites, National Satellite Meteorological Center, China Meteorological Administration, Beijing, 100081, China

[3]Institute of Heavy Rain, China Meteorological Administration, Wuhan, 430205, China

Correspondence: Yunfei Fu (fyf@ustc.edu.cn)

Abstract. ~~Rain cells are~~Understanding the characteristics of rain cell, the most ~~common units~~basic unit in ~~the~~ natural precipitation system~~. Enhancing the understanding of these rain cell characteristics can significantly~~, is helpful to improve the cognition of the precipitation system. ~~Previous studies have mostly analyzed rain cells from a single radar data.~~ In this study, ~~we~~based on the merged ~~the~~data of precipitation ~~parameters measured~~profile data, reflectivity and infrared data, and microwave brightness temperature data, which were observed by the Tropical Rainfall Measuring Mission (TRMM) precipitation radar (PR~~)~~ ~~with the muti-channel cloud-top radiance measured by the)~~, visible and infrared scanner (VIRS) and ~~the muti-channel brightness temperature measured by the~~ TRMM microwave imager (TMI~~). The~~), rain cells were identified ~~within~~in the PR ~~orbit, and the~~ swath ~~truncation effect was eliminated. We used~~ by two methods ~~for rain cell identification:~~, the minimum bounding rectangle (MBR) method and the best fit ellipse (BFE) method~~, and compared the differences between these two methods in describing the rain cell characteristics. The results indicate that both methods can better reflect the~~. The geometric ~~characteristics of rain cells. Compared with the MBR method, the BFE method can obtain a smaller rain cell area,~~ and ~~the filling ratio is better. However, the MBR method can simplify the data storage volume. Consequently, we employed the MBR method to analyze the precipitation structure~~ physical parameters of ~~two typical rain cell precipitation cases. The results show that the new rain cell dataset can be used for~~

设置了格式: 字体: 17 磅, 加粗
设置了格式: 字体: 17 磅, 加粗
带格式的: 两端对齐, 段落间距段前: 18 磅, 行距: 固定值 22 磅
设置了格式: 字体: 17 磅, 加粗
设置了格式: 字体: 17 磅, 加粗
设置了格式: 字体: 17 磅, 加粗
设置了格式: 字体: 小四, 非加粗
带格式的: 两端对齐, 段落间距段前: 9 磅
设置了格式: 字体: 小四, 非加粗, 字体颜色: 文字 1
设置了格式: 字体: 小四, 非加粗, 字体颜色: 文字 1
设置了格式: 字体: 小四, 非加粗
设置了格式: 字体: 小四, 非加粗
设置了格式: 字体: 10 磅
带格式的: 两端对齐, 段落间距段前: 6 磅
设置了格式: 字体: 10 磅
设置了格式: 字体: 非加粗, 倾斜, 字体颜色: 自动设置
带格式的: Correspondence, 左
设置了格式: 字体: 10 磅, 倾斜, 字体颜色: 自动设置
设置了格式: 字体: 10 磅
设置了格式: 字体: 10 磅, 倾斜
设置了格式: 字体颜色: 自动设置
设置了格式: 字体: 加粗, 字体颜色: 自动设置

~~the analysis of rain cell precipitation~~rain cell were also defined. By analyzing the geometric parameters (length, width, height and so on) and physical parameters (rain rate, visible~~/infrared and microwave signals, which provides valuable data for comprehensive studies on the~~ reflectivity and thermal infrared brightness temperature from cloud top, and microwave brightness temperature from cloud column) of two rain cells (weak rain cell and strong rain cell) identified by MBR method and BFE method, results indicate that the strong rain cell is filled with deep convective precipitation and also has low thermal infrared bright temperature in cloud top, while the weak rain cell is stratiform precipitation with small rain rate. Compared to the BFE method, the MBR method has a smaller rain cell length, while both methods demonstrate similar rain cell ~~structural characteristics and furthers the understanding~~ widths. The filling ratio of ~~precipitation mechanisms.~~BFE method is slightly higher than that of MBR method. In general, the both methods indicate that the rain cell identification and the defined rain cell parameters are reasonable and intuitive. The data which were used in this paper are freely available at ~~https://doi.org/10.5281/zenodo.8352587~~https://doi.org/10.5281/zenodo.13118878 (Wu ~~et al., 2023~~and Fu, 2024).

设置了格式: 字体颜色: 自动设置

1 Introduction

设置了格式: 字体: 10 磅, 加粗, 字体颜色: 自动设置

带格式的: 1 级, 段落间距段前: 24 磅, 段后: 12 磅

Precipitation is an important part of the global energy and water cycle (Houze, 1997; Oki and Kanae, 2006; Lau and Wu, 2010). ~~Rain cells are considered as~~In the ~~most basic~~ water cycle, the rain cell that constitutes a precipitation ~~unit, but they have been defined differently in literatures.~~system can be considered the most elementary unit in different definitions. The investigation of the three-dimensional structure of rain cell is helpful to understand the thermodynamic structure and microphysical processes within precipitation systems (Houze, 1981; Zipser and Lutz, 1994; Yuter and Houze, 1995; Fu and Liu, 2001). Austin and Houze (1972) ~~studied the precipitation patterns in New England and~~ found ~~that there are basically composed of~~ subsynoptic scale precipitation regions~~.~~, that each ~~with~~had rather clearly definable characteristics and behavior~~.~~ when they studied the precipitation patterns in New England. Based on radar observations and ~~detailed~~ rain gauge records, ~~the precipitation patterns can be~~ they also divided precipitation pattern into synoptic areas, large mesoscale areas, small mesoscale areas and cells. The rain cell with ~~an~~ area of about 10 km^2 in radar echo ~~is~~was regarded as a single cumulus convective

unit in their study~~. Goldhirsh and Musiani ((Gagin et al., 1986) defined rain cell as areas with rain rates greater than or equal to ; Capsoni et al., 1987).~~

More studies were done by defining the threshold ~~by setting a correspondingof~~ rain ~~rate~~ cell, such as an area where rain rates were greater than a given threshold~~.~~ (Goldhirsh and Musiani, 1986). For example, Capsoni et al. (1987) defined rain cell as the connected region with rain rate greater than 5 mm h^{-1} based on S-band radar observation near Milan in 1980. Awaka (1989) modified rain rate threshold to 0.4 mm h^{-1}. Meanwhile, many ~~papers studied~~studies exposed the relationship between ~~precipitation~~rain rate threshold and rain cell size based on ground-based radar data (Konrad, 1978; Sauvageot et al., 1999; Feral et al., 2000; Begum and Otung, 2009). ~~Capsoni et al. (1987) defined rain cell as a connected region with a precipitation rate greater than 5 mm h^{-1} based on S-band radar observation near Milan in 1980, and obtained the relationship between the spatial number densities of rain cells and the cumulative distribution of precipitation rate. Awaka (1989) modified the precipitation rate threshold to 0.4 mm h^{-1}.~~

~~In order to obtain the shape parameters,~~ Feral et al. (2000) ~~employed the~~adopted elliptic fitting method to investigate the geometric characteristics and directional distribution of rain ~~cells~~cell. The statistical results also revealed that the major axis length was twice longer than the minor axis length ~~for the majority of the rain cells,~~ and the direction distribution was uniform~~. When studying~~ in the majority of the rain cells.

Since the ~~horizontal dimensions~~late 1990s, observations of ~~the~~ precipitation ~~systems, Nesbitt et al. (2006) used the best-fit ellipse method to obtain the major axis~~radar (PR), visible and ~~minor axis. However, due to the limitation of the swath width, some~~ infrared scanner (VIRS) and TRMM microwave imager (TMI) aboard the TRMM satellite provided a wealth of data for systematical study cloud and precipitation (Kummerow et al., 1998, 2000; Nesbitt et al., ~~systems were truncated. The results indicated that there were obvious differences of storm morphology characteristics over land and ocean, which may lead to significant differences in regional precipitation simulation.~~2000; Viltard et al., 2000; Liu and Fu, 2001; He et al., 2006; Schumacher and Houze, 2003; Li and Fu, 2005; Liu and Fu, 2010; Fu, 2014). With the massive data observed by PR, VIRS and TMI, Nesbitt et al. (2006), Liu et al (2007, 2008), and Liu and Zipser (2013) ~~investigated the different horizontal structures of convective precipitation systems~~made spick-and-span studies in the ~~tropics and subtropics by using 14 years of Tropical Rainfall Measuring Mission (TRMM) Precipitation Radar (PR) observations combined~~field of

rain cell identification and its parameters with ~~the best ellipse~~elliptic fitting method. ~~They found~~Their rain cell data were also widely used on analyzing the temporal and spatial distribution characteristics of rain cell (Zhou et al., 2013; Yokoyama et al., 2014; Ni et al., 2015), such as that line shaped convective systems occurred more frequently over ocean, and showed higher frequency in the subtropics (Liu and Zipser, 2013). To continue reveal the characteristics of rain cell parameters, Fu et al. (2020) defined the geometric and physical parameters of rain cell, used the minimum bounding rectangle (MBR) method to identify the rain cell within the width of the PR scan, calculated these parameters and obtained their characteristics. The data of rain cell generated from MBR method was applied to study the morphological characteristics of rain cell in summer Tibetan Plateau (Chen et al., 2021). Cai et al. (2024) adopted the three methods, minimum circumscribed ellipse, minimum bounding rectangle and direct indexing area, for rain cell fitting. They also compared the geometric characteristics generated from the three methods.

~~Fu et al. (2020)~~However, the rain cell data identified by MBR method need to add reflectivity and infrared temperature observed by VIRS and microwave bright temperature measured by TMI, which will give full play to the advantages of TRMM instruments. For the above purposes, our study merged observation data of PR, VIRS and TMI at PR pixel resolution, then used two methods, the minimum bounding rectangle (MBR) method and the best fit ellipse (BFE) method, to identify rain ~~cells and studied the geometric and physical parameter characteristics of rain cells over tropical land and ocean areas with 15 yr measurements of the TRMM PR. The study showed that the average rain rate of rain cells is more frequently related to the increase of area, and the increasing rate over land is greater than that over ocean. Chen et al. (2021) used the same~~ cell and produce a new dataset ~~in the above study to analyze the multidimensional morphological characteristics of~~ with precipitation ~~areas over the Tibetan Plateau in summer, and found that there is a close relationship between the morphological characteristics of precipitation areas and the intensity of precipitation.~~

~~The investigation of the three-dimensional~~ parameter, visible/infrared and microwave signal. The structure of ~~rain cells is helpful to understand the thermodynamic structure and microphysical processes within precipitation systems (Houze, 1981; Zipser and Lutz, 1994; Yuter and Houze, 1995; Liu and Fu, 2001). The PR onboard the TRMM provides an excellent opportunity to study the 3D structure of precipitation (Kummerow et al.,~~ this study is as follows: section 2 describes data and data~~1998, 2000; Nesbitt et al.,~~ 1999; Schumacher and Houze, 2003; Li and Fu, 2005), and the visible and infrared scanner

~~(VIRS) on the satellite can provide spectral signals and cloud parameters information on the top of precipitation clouds (Liu and Fu, 2010; Fu, 2014), the TRMM microwave imager (TMI) can provide information of different phase particles inside precipitation clouds (Viltard et al., 2000; He et al., 2006; Fu et al., 2021).~~

~~Fu et al. (2007a) analyzed the characteristics of precipitating and non-precipitating clouds in typhoon Ranan occurred in August 2004 by matching and~~ merging ~~data measured by TRMM PR, TMI and VIRS. The result indicated that large particles are mostly in the precipitation cloud, and the effective radius distribution of non-precipitating cloud particles is relatively wide. Fu et al (2007b) utilized the results of multi-instrument measurements on TRMM to analyze several typical precipitation systems over the East Asia, and reveal the relationship of precipitation structure, lightning activities, precipitation cloud top and rainfall rate near surface. Liu et al (2008) established a precipitation feature database based on 9 years of TRMM observation data, matching the VIRS and TMI observation results to PR pixels resolution. Subsequently, Liu et al (2009) used this database to study the contribution of warm rain systems to precipitation over the tropics and obtained the seasonal and spatial distribution of warm rain systems.~~

~~This paper is merging the PR, VIRS, and TMI measurements at PR pixel resolution, and combining the rain cell~~ methods, section 3 introduces rain cell identification method ~~to establish a new precipitation parameter and visible/infrared and microwave signal dataset. Section 2 describes the data and merging methods. Section 3 introduces the definition method of rain cells and identification method. Section~~, section 4 defines the geometric and physical parameters of rain ~~cells. In Section 5, the statistical results of rain~~ cell ~~parameters are given and the structures of~~, section 5 analyzes two typical rain cells ~~are analyzed~~in geometric and physical parameters. Access to the datasets is introduced in ~~Sect.~~section 6, and conclusions are presented in ~~Sect.~~section 7.

2 Data

设置了格式: 字体: 10 磅, 加粗, 字体颜色: 自动设置

带格式的: 1 级, 段落间距段前: 24 磅, 段后: 12 磅

~~2.1 Tropical Rainfall Measuring Mission~~

The TRMM was jointly developed by the US National Aeronautics and Space Administration (NASA) and the Japan Aerospace Exploration Agency (JAXA) and launched on November 27, 1997. The TRMM is a non-solar synchronous polar-orbiting satellite with an orbital inclination of 35° and observes a location between 38° S and 38° N (Simpson et al., 1996; Kummerow et al., 1998, 2000). The satellite carries five instruments: PR, VIRS, TMI, the Lighting Imaging Sensor (LIS), the Cloud and Earth

Radiant Energy Sensor (CERES). This study mainly involves the measurements of TRMM PR, VIRS, and TMI.

2.~~2~~1 PR ~~and~~data 2A25 ~~dataset~~

The PR was the first spaceborne precipitation radar onboard the TRMM. It is a single-frequency microwave radar with a frequency of 13.8 GHz (Kummerow et al., 1998; Kozu et al., 2001). PR scans in the cross-track direction with a scanning inclination of 17°. There are 49 pixels on each scanning line. The horizontal resolution is about 4.3 km at nadir (5.0 km after the orbital boost), and the scanning width is 215 km (245 km after the orbital boost). It can detect the three-dimensional structure of precipitation from mean sea level to 20 km (a total of 80 layers) with a vertical resolution of 0.25 km.

The 2A25 data is the second-level data product of the TRMM PR, which is generated by inverting the echo signals detected by the PR. This dataset mainly includes scanning time, geographic information, three-dimensional rain rate, rain type and so on (Awaka et al., 1997). The detection sensitivity of the PR is about 17 dBZ, corresponding to the rain rate of about 0.4 $\mathrm{mm\ h^{-1}}$ (Schumacher and Houze, 2003). Therefore, when the rain rate of the pixels is lower than 0.4 $\mathrm{mm\ h^{-1}}$, the default value is set and will not be involved in the calculation.

2.~~3~~2 VIRS ~~and~~data 1B01 ~~dataset~~

The VIRS scans in the cross-track direction with a scanning angle of 45°. There are 261 pixels on each scanning line. The scanning width is 720 km (833 km after the orbital boost), and the horizontal resolution is 2.2 km at nadir (2.4 km after the orbital boost). It has five channels from visible to the far infrared band: CH1 (0.63 μm), CH2 (1.6 μm), CH3 (3.7 μm), CH4 (10.8 μm) and CH5 (12.0 μm). The 1B01 is a first-level data product of VIRS, which includes the reflectivity at CH1 and CH2, the infrared radiation brightness temperature at CH3, CH4, and CH5 after the correction and calibration of the VIRS detection results.

~~The 1B01 is a first-level data product of VIRS, which includes the reflectivity (RF1, RF2) and the infrared radiation brightness temperature ($TB_{3.7}$, $TB_{10.8}$, $TB_{12.0}$) after the correction and calibration of the VIRS detection results.~~

设置了格式: 字体: 10 磅, 加粗, 字体颜色: 自动设置
带格式的: 2 级, 段落间距段前: 12 磅, 段后: 12 磅
设置了格式: 字体: 10 磅, 加粗, 字体颜色: 自动设置
设置了格式: 字体: 10 磅, 加粗, 字体颜色: 自动设置
设置了格式: 字体: 10 磅, 加粗, 字体颜色: 自动设置

设置了格式: 字体: 10 磅, 加粗, 字体颜色: 自动设置
设置了格式: 字体: 10 磅, 加粗, 字体颜色: 自动设置
设置了格式: 字体: 10 磅, 加粗, 字体颜色: 自动设置
设置了格式: 字体: 10 磅, 加粗, 字体颜色: 自动设置
带格式的: 2 级, 段落间距段前: 12 磅, 段后: 12 磅

2.43 TMI ~~and~~data 1B11 ~~dataset~~

The TMI is a nine-channel passive microwave radiometer with five frequencies spanning from 10 to 85 GHz. The microwave signal frequencies are 10.65 GHz, 19.35 GHz, 21.3 GHz, 37.0 GHz, and 85.5 GHz, except for 21.3 GHz, which is a single vertical polarization channel. The other four frequencies are horizontal (H) and vertical (V) polarization dual channels. The scanning width is 760 km (878 km after the orbital boost). The horizontal resolution of each frequency channel (effective field of view of beam, Kummerow et al., 1998) varies from 63 km × 37 km at 10.65 GHz to 7 km × 5 km at 85.5 GHz. The 1B11 data contains the calibrated TMI-detected microwave brightness temperature at multiple channels.

2.~~5~~4 The merged data of 2A25, 1B01 and 1B11 ~~merged data~~

To comprehensively analyze the parameters of precipitation, cloud top spectral signal and particle phase in ~~the cloud~~ precipitation system, the rain rate profile and echo profile of 2A25, the reflective and infrared temperature of 1B01 ~~and~~ , and the microwave brightness temperature of 1B11 ~~data products (derived from the TRMM PR, VIRS and TMI, respectively)~~ were ~~matched and~~ collocated in PR horizontal resolution and produced a merged~~. Due to~~ data. The reason for that is because the difference ~~in data detection methods, the~~ spatial resolution ~~is different for~~ of the three instruments, but the time lag ~~between detections~~ of observation among the three instruments to the same target is less than ~~1 min. It provides the possibility of data merging because of~~ 1min, i.e. the quasi-synchronous ~~detection. In this paper, we default to the consistency of time during data merging, only considering spatial merging. Based on the pixel resolution of PR detection, VIRS and TMI are matched to corresponding pixels according to latitude and longitude~~observations (Liu et al., 2008; Fu et al., 2011; Sun and Fu, 2021).

~~For the PR and VIRS, in order to obtain the spectral signals (reflectivity and infrared radiation brightness temperature) near the precipitation cloud top, the horizontal resolution of 1B01 pixel is decreased to make it consistent with 2A25. Generally, there are usually~~ Statistics showed about 7 VIRS pixels ~~near 1 PR pixel. The specific method is to introduce the Gaussian function. The spectral signals are calculated by weighted averaging the VIRS near the PR pixel.~~within 1 PR pixel. It was found that the spectral signals of VIRS changed weakly after merging, the mean change was less than 0.7 %, and the

设置了格式: 字体: 10 磅, 加粗, 字体颜色: 自动设置
带格式的: 2 级, 段落间距段前: 12 磅, 段后: 12 磅
设置了格式: 字体: 10 磅, 加粗, 字体颜色: 自动设置
设置了格式: 字体: 10 磅, 加粗, 字体颜色: 自动设置
设置了格式: 字体: 10 磅, 加粗, 字体颜色: 自动设置
设置了格式: 字体: 10 磅, 加粗, 字体颜色: 自动设置
设置了格式: 字体: 10 磅, 加粗, 字体颜色: 自动设置
设置了格式: 字体: 10 磅, 加粗, 字体颜色: 自动设置
带格式的: 2 级, 段落间距段前: 12 磅, 段后: 12 磅

mean square deviation was less than 2.5 % (Fu et al., 2011). ~~Sun and Fu (2021) considered the merging process between the PR and VIRS pixels was no dramatic variations on the original data, and the conclusions were consistent with Fu et al. (2011).~~

~~For TMI, the measured values in different bands~~Due to TMI channels have different spatial resolutions~~.~~ ~~In order~~ that is larger than PR pixel resolution, the nearest neighbor method was used to obtain ~~the~~ microwave~~ radiation~~ brightness temperature ~~in~~at PR pixel resolution, ~~it is necessary to increase the horizontal resolution of 1B11 pixels to make it consistent with the resolution of 2A25 pixels. By using the nearest neighbor method,~~i.e. each PR pixel ~~is~~was assigned the microwave brightness temperatures of nine channels a TMI pixel closest to ~~it~~the PR pixel (Liu et al., 2008).

3 ~~Algorithm~~The algorithm of rain cell identification

~~Previous studies have pointed out that the measurements of PR are inevitably affected by the swath truncation effect due to the limitation of the PR detection orbit. Nesbitt et al. (2006) analyzed 3-year TRMM PR data and concluded that nearly 42% of total rainfall is affected by the swath truncation. Liu and Zipser (2013) showed that due to the influence of swath truncation, the parameters described rain cell would be distorted and the captured precipitation systems would be incomplete. Fu et al. (2020) defined rain cell as neighboring rain pixels with at least 0.4 mm h^{-1} near-surface rain rate or 17 dBZ reflectivity by using the PR data.~~ The ~~rain cells affected by the swath truncation were removed in the study, and the rain cells completely detected by PR swath were retained.~~

~~This paper also adopts the same~~ definition ~~and elimination method~~ of rain ~~cells~~cell in this study is the same as that proposed by Fu et al. (2020), i.e. a rain cell consists of at least four ~~(2020). Firstly, using the eight~~ connected ~~region method identifies the continuous region of rain~~rain pixels within the swath of PR scan. According to the working mode of PR, its swath consists of 49 pixels~~. For example, for any rain pixel A, iteratively search its neighboring pixels (a total of 8 pixels). If one or more of them are also rain pixels (marked as B, C, …), A, B, C and … are~~ (from number 1 to 49), so if the identified ~~as the same~~ rain cell~~. Then, the search process is repeated for B, C, … rain~~ has pixels ~~until all adjacent pixels~~at the edge of ~~any rain~~the PR swath (the first pixel ~~in~~and 49th pixel), the rain cell ~~are non-precipitation pixels. Upon completion of the identification process for a rain cell,~~is not included. If the identified rain cell is ~~numbered. Secondly, the rain pixel swath truncation identification and the elimination of micro-rain cells~~

带格式的: 缩进: 首行缩进: 0 字符

设置了格式: 字体: 10 磅, 加粗, 字体颜色: 自动设置

设置了格式: 字体: 10 磅, 加粗, 字体颜色: 自动设置

带格式的: 1 级, 段落间距段前: 24 磅, 段后: 12 磅

~~(less than 4 pixels) are executed.~~at the beginning and end of the PR swath, the rain cell is also eliminated. The ~~identified rain cells are systematically traversed. When a rain cell edge is identified as located at the edge of the track, it~~advantage of this is ~~defined as a truncated rain cell. If the number of pixels in a rain cell is less than 4, it is defined as a micro rain cell. The above rain cells will be removed (Chen, 2019).~~ to avoid the truncation effect of PR swath. To ~~describe~~automatically identify rain cell in the ~~shape of~~merged data, the ~~rain cell,~~best fit ellipse (BFE) method and the minimum bounding rectangle (MBR) ~~rain cell identification method and the best fit ellipse (BFE) rain cell identification method are~~ method were used~~ to identify the rain cell. The MBR rain cell identification method is to find the~~. The two methods can calculate an ellipse and a rectangle with the smallest area covering the target object (rain cell), respectively, as did by Nesbitt et al. (2006) and Fu et al. (2020). ~~) by rotating the external rectangle (Fu et al., 2020). The BEF rain cell identification method fits the most suitable elliptical shape wrapped rain cell according to the polygonal connection frame of the outer boundary of the rain cell (Nesbitt et al., 2006).~~

~~4 Definitions of parameters of rain cell~~

~~We define some~~ The slight differences of geometric ~~and~~ parameters calculated by MBR method and BFE method show in the length and width of rain cell, while the physical parameters ~~to describe~~calculated by the both methods are the same. The rain cell parameters identified ~~rain cells (~~by the two methods presented in this study can be used by studies according to their own preferences.

4 The definitions of rain cell parameters

The definition of geometric and physical parameters describing the identified rain cell was almost the same as that of Fu et al~~.,~~. (2020). The specific geometric parameters ~~are~~were listed in Table 1, ~~where~~in which the first six parameters ~~are called~~descript the horizontal ~~geometric parameters~~geometry of rain cell and the rest ~~are~~do the vertical ~~geometric parameters. The differences in geometric~~geometry. These parameters ~~of the MBR method and the BFE method are studied. Where~~ have a clear physical meaning, such as α represents the horizontal shape of ~~the~~ rain cell, a small (large) α indicates that the ~~two-dimensional~~horizontal shape of ~~the~~ rain cell is more like a strip (square) precipitation system, and has more (less) correlation with a frontal precipitation system. The variable β expresses the ratio of ~~the~~ rain cell area (~~S_{rain}~~)S_{rain}) to the area of the ~~identification~~MBR or BFE frame (~~S~~S), and characterizes the

~~internal organization within the~~effectiveness of both methods used to identify rain cell. Large (small) β ~~suggests that those rain pixels are more (less) compactly organized, and are more (less) likely to be associated with strong convective systems.~~indicates more (less) rain pixels inside the MBR or BFE frame. The variables ~~γ_{max}~~γ_{max} and ~~γ_{av}~~γ_{av} represent the three-dimensional spatial shape of ~~the~~ rain cell. Small ~~γ_{max}~~γ_{max} (~~γ_{av}~~γ_{av}) indicates a "squatty" appearance of rain cell, in contrast to a "lanky" appearance for large ~~γ_{max}~~γ_{max} (~~γ_{av}~~γ_{av}).

Table 1. ~~**Definitions of geometric parameters**~~**Geometric parameter definitions of rain cell**~~,~~ **by the minimum bounding rectangle (MBR) method and the best fit ellipse (BFE) method**

~~Symbol~~Parameters in MBR method		~~Geometric meaning of rectangle~~Parameters in BFE method	~~Geometric meaning of ellipse~~
~~L (km)~~L_r (km), length	~~r_L (km) Length of the MBR method~~	~~e_L~~(L_e (km~~)~~ Length), length of the major axis ~~of the BFE method~~	
~~W (km)~~W_r (km), width	~~r_W (km) Width of the MBR method~~	~~e_W~~(W_e (km~~)~~ Width), length of the minor axis ~~of the BFE method~~	
~~α~~	~~r_α~~ Horizontal shape of rain cell, ~~$r_\alpha = r_W/r_L$~~α_r, horizontal shape index, $\alpha_r = W_r/L_r$	~~e_α~~ Horizontal shape of rain cell, ~~$e_\alpha = e_W/e_L$~~α_e, horizontal shape index, $\alpha_e = W_e/L_e$	
~~S_{rain} (km^2)~~ ~~S~~S_r (km^2~~)~~, MBR area, $S_r = L_r * W_r$	Area of the rain cell, sum of all areas of rain pixels ~~r_S (km^2) Area of the MBR method, $r_S = r_L * r_W$~~	~~e_S (km^2) Area of the BFE method, $e_S = \frac{\pi}{4} * e_L * e_W$~~$S_e$ (km^2), BFE area, $S_e = \frac{\pi}{4} * L_e * W_e$	
β_r, filling ratio, $\beta_r = S_{rain}/S_r$	~~β~~ ~~r_β~~ ~~Filling ratio~~S_{rain} (km^2), rain area, sum of ~~the~~all rain pixel areas in rain cell~~, $r_\beta = S_{rain}/r_S$~~	β_e, filling ratio, $\beta_e = S_{rain}/S_e$ ~~e_β~~ ~~Filling ratio of the rain cell, $e_\beta = S_{rain}/e_S$~~	
~~H_{max} (km)~~	~~Maximum~~H_{max} (km), maximum echo top height ~~among rain pixels~~ in ~~the~~ rain cell		
~~H_{av} (km)~~	~~Mean~~H_{av} (km), mean echo top height ~~averaged among rain pixels~~ in ~~the~~ rain cell		
~~γ_{max}~~	~~Maximum~~γ_{max}, maximum spatial morphology~~, $\gamma_{max} = H_{max}/L$~~ index of rain cell, $\gamma_{max} = H_{max}/l$		
~~γ_{av}~~	~~Mean~~γ_{av}, mean spatial morphology~~, γ_{av}~~ index of rain cell, $\gamma_{av} = 2$~~$H_{av}/(L + W)$~~$H_{av}/(L + W)$		
~~H_{avc} (km)~~	~~Mean~~H_{avc} (km), mean echo top height of convective precipitation in ~~the~~ rain cell		

带格式的: 段落间距段后: 10 磅
删除的单元格
格式化表格
设置了格式: 字体: +西文正文 (等线), 五号
设置了格式: 字体: +西文正文 (等线), 五号
设置了格式: 字体: +西文正文 (等线), 五号
删除的单元格
设置了格式: 字体: +西文正文 (等线), 五号
设置了格式: 字体: +西文正文 (等线), 五号
设置了格式: 字体: +西文正文 (等线), 五号
删除的单元格
设置了格式: 字体: +西文正文 (等线), 五号
设置了格式: 字体: +西文正文 (等线), 五号
删除的单元格
删除的单元格
格式化表格
设置了格式: 字体: +西文正文 (等线), 五号
设置了格式: 字体: +西文正文 (等线), 五号
删除的单元格
删除的单元格
格式化表格
设置了格式: 字体: 等线
设置了格式: 字体: 等线
设置了格式: 字体: 等线
设置了格式: 字体: 等线
设置了格式: 字体: 等线
设置了格式: 字体: 等线

~~H_{avs} (km)~~	~~Mean~~H_{avs} (km), mean echo top height of stratiform precipitation in ~~the~~ rain cell
H_dBZ$_{max}$ (km), height of the maximum reflectivity factor in rain cell	
μ, ratio of the maximum reflectivity factor height to the maximum echo top height in rain cell	

~~Since the~~ The physical parameter definitions of rain cell ~~dataset contains the measurements of multiple instruments, we define some physical parameters (~~by MBR method and BFE method were listed in Table 2~~) based on~~ including rain type, rain rate ~~profiles, near surface~~profile, reflectivity factor profile, mean rain ~~rates~~rate, visible reflectivity and infrared brightness temperature, microwave brightness temperature and so on. Those parameters are significant to represent the intensity, the inhomogeneity, and the evolution stage of rain ~~cells~~cell.

Table 2. ~~Definitions of physical parameters~~Physical parameter definitions of rain cell by the minimum bounding rectangle (MBR) method and the best fit ellipse (BFE) method.

Symbol	Physical meaning
RR_{ave} (mm h^{-1})	Mean rain rate ~~obtained by averaging all rain rates within the~~in rain cell
RR_{max} (mm h^{-1})	Maximum rain rate ~~among rain pixels of the~~in rain cell
RR_{avc} (mm h^{-1})	Mean convective rain rate ~~averaged by all convective rain rates within~~in rain cell
RR_{avs} (mm h^{-1})	Mean stratiform rain rate ~~averaged by all stratiform rain rate within~~in rain cell
RR_{maxc} (mm h^{-1})	Maximum rain rate ~~among~~of convective ~~pixels of the~~precipitation in rain cell
RR_{maxs} (mm h^{-1})	Maximum rain rate ~~among~~of stratiform ~~pixels of the~~precipitation in rain cell
CAF (%)	~~Fraction of convective~~Convective area fraction to total precipitation area ~~within the~~in rain cell
SAF (%)	~~Fraction of stratiform~~Stratiform area fraction to total precipitation area ~~within the~~in rain cell
CPC (%)	Convective precipitation contribution to total precipitation ~~within the~~in rain cell
SPC (%)	Stratiform precipitation contribution to total precipitation ~~within the~~in rain cell
dBZ_{max} (dBZ)	Maximum ~~radar~~ reflectivity factor ~~among rain pixels of the~~in rain cell
~~H_dBZ_{max} (km)~~	~~Height of the maximum radar reflectivity factor among rain pixels of the rain cell~~
RF_{ave}	Mean reflectivity ~~obtained by averaging all reflectivities~~ of VIRS visible or near infrared channel ~~within the~~in rain cell
RF_{avc}	Mean ~~convective~~ reflectivity ~~averaged by all convective reflectivities~~ of VIRS visible or near infrared channel ~~within the~~for convective precipitation in rain cell
RF_{avs}	Mean ~~stratiform~~ reflectivity ~~averaged by all stratiform reflectivities~~ of VIRS visible or near infrared channel ~~within the~~for stratiform precipitation in rain cell
TB_{ave} (K)	Mean brightness temperature ~~obtained by averaging all brightness temperatures~~ of VIRS mid-infrared and far-infrared, TMI channel ~~within the~~in rain cell

带格式的: 段落间距段后: 10 磅
设置了格式: 字体颜色: 文字 1

TB_{avc} (K)	Mean brightness temperature ~~averaged by all~~of VIRS mid-infrared and far-infrared, TMI channel for convective ~~brightness temperatures of channel within the~~precipitation in rain cell
TB_{avs} (K)	Mean brightness temperature ~~averaged by all~~of VIRS mid-infrared and far-infrared, TMI channel for stratiform ~~brightness temperatures of channel within the~~precipitation in rain cell

5 Results

5.1 ~~Statistics of rain cell~~Precipitation parameters of rain cell

~~In this study, we select two methods for identifying rain cells. It is important to note that the choice of identification method may influence the results of parameters. Taking the two rain cells shown in Figure 1 as example, they locate on the southern slope of the Tibetan Plateau (orbit 08691 on 2 June, 1999) and the eastern part of the Tibetan Plateau (orbit 31787 on 13 June, 2003), respectively. Table 3 shows the calculated horizontal geometric parameters of the rain cells displayed in Fig. 1.~~

~~The first case shown in Fig. 1a is calculated by the MBR method with r_L = 290.86 km, r_W = 140.29 km, S_{rain} = 10223.5 km², r_s = 40803.36 km², and r_β = 0.25, which shows a strip shape (r_α = 0.48). For the second case (Fig. 1b), r_L, r_W, S_{rain}, r_s, and r_α are 169.57 km, 76.18 km, 4496.4 km², 12917.48 km², and 0.45, respectively. In addition, the filling ratio in the second case (0.35) is slightly larger than that in the first case (0.25), resulting in a more compact rain cell system overall.~~

设置了格式: 字体颜色: 文字 1
设置了格式: 字体颜色: 文字 1
设置了格式: 字体颜色: 文字 1
设置了格式: 字体颜色: 文字 1
设置了格式: 字体颜色: 文字 1
设置了格式: 字体颜色: 文字 1
设置了格式: 字体颜色: 文字 1
设置了格式: 字体颜色: 文字 1
设置了格式: 字体: 10 磅, 加粗, 字体颜色: 自动设置
带格式的: 1 级, 段落间距段前: 24 磅, 段后: 12 磅
带格式的: 2 级, 段落间距段前: 12 磅, 段后: 12 磅
设置了格式: 字体: 10 磅, 加粗, 字体颜色: 自动设置
设置了格式: 字体: 10 磅, 加粗, 字体颜色: 自动设置

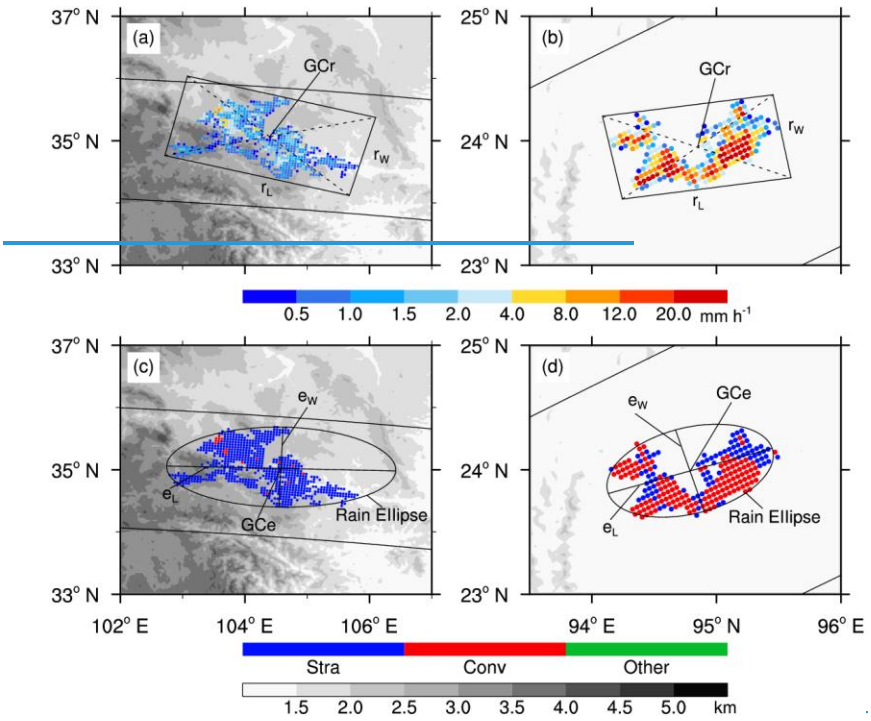

~~Figure 1. Near surface rain rate of two rain cells that occurred on 2 June~~In order to better understand the geometric and physical parameters of the defined rain cell identified by MBR method and BFE method, two rain cells were analyzed below. One identified rain cell A, occurred on 2 June, 1999 in southern Tibetan Plateau (TRMM orbit 08691), and the other, rain cell B, on 13 June, 2003 in eastern Tibetan Plateau (TRMM orbit 31787). Figure 1 shows the distribution of rain rate and rain type for the two rain cells, the frame of both MBR and BFE is also plotted, which clearly showed the length and width of MBR method, and the long and short axis of BFE method. Statistics of parameters for the two rain cells shows in Table 3. Figure 1a shows that rain cell A identified by MBR method has length 290.86 km (L_r), width 140.29 km (W_r), rain area 10223.5 km^2 (S_{rain}), MBR area 40803.36 km^2 (S_r), and filling ratio 0.25 (β_r). The horizontal shape index is 0.48 (α_r), which indicates rain cell A with a strip like shape. The rain cell A identified by BFE method (Figure 1c) has length 347.63 km (L_e), width 139.94 km (W_e), rain area 10223.5 km^2 (S_{rain}), BFE area 38207.27 km^2 (S_e), and filling ratio 0.27 (β_e). The horizontal shape index is 0.4 (α_e), which also indicates rain cell A with a strip like shape. The rain cell B identified by MBR method and BFE method showed in Figure 1b and 1d, its parameters listed in Table 3 show it

slightly like strip shape.

The vertical parameters of the both rain cells identified by the both methods listed in Table 3 show no differences in method because statistics were made in rain pixels inside rain cell. Comparing rain cell A and B, the latter has higher echo top (H_{max} = 17.75 km, H_{av} = 9.47 km), and shows like "lanky" appearance (γ_{max} = 0.11, γ_{av} = 0.08). In rain cell B, the mean echo top height of convective precipitation and stratiform precipitation, 10.39 km and 7.96 km, is also higher than that in rain cell A, which indicates that the updraft velocity within rain cell B is strong and the precipitating cloud is deep. The ratio of the maximum reflectivity factor height to the maximum echo top height μ is 0.37 and 0.15 for rain cell A and B, respectively. Combining γ_{max} and μ it can be concluded that rain cell B is a deep precipitation system with large particles in the lower part of cloud.

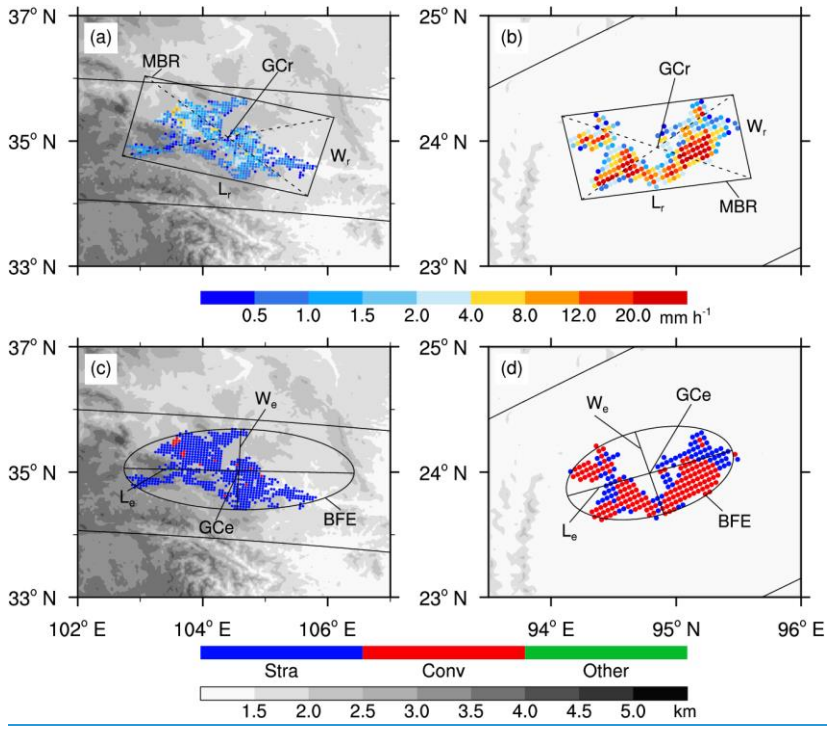

Figure 1. Two rain cells occurred on June 2, 1999 (a) and on 13 June 13, 2003 (b) measured by PR. In: rain rate (a and b) and rain type (c, and d), rain pixels with , blue, red, and green represent for stratiform, convective, and other precipitation, respectively). The two rain cells in up panel were identified by MBR method, in bottom by BFE method. GCr and GCe represent for geometric center of rain cell identified by MBR method and BFE method, respectively. The identification boxes are captured by the MBR method (a, b) and the BFE method (c, d) for two rain cells The gray level in the figure represents the elevation of the

带格式的: 段落间距段后: 10 磅

terrain.

~~The first case (Fig. 1c) is calculated by the BFE method with e_L = 347.63 km, e_W = 139.94 km, e_S = 38207.27 km², e_α = 0.4, and e_β = 0.27. For the second case (Fig. 1d), e_L, e_W, e_S, e_α, and e_β are 170.66 km, 76.76 km, 10289.43 km², 0.45, and 0.44, respectively. Based on the horizontal geometric parameters of rain cells captured by the MBR and BFE method, it is evident that the area of the rectangular box is larger than that of the ellipse box. This difference in area results in a smaller filling ratio for the MBR method as compared to the BFE method. There is no significant difference between the two methods in terms of other geometric parameters. In practical application, compared with the BFE method, the MBR method can greatly simplify the amount of data storage. Moreover, the MBR method can envelop all the pixels of the rain system, which works better than the BFE method in bow precipitation and small precipitation system (Chen, 2019).~~

~~**Table 3. The horizontal geometric parameters of the first/second case calculated by MBR and BFE.**~~

The physical parameters of the both rain cells identified by the both methods were listed in Table 4. PR observation showed that the mean rain rate RR_{ave} and the maximum rain rate RR_{max} of rain cell B were 11.64 mm h^{-1} and 113.14 mm h^{-1}, respectively, and rain cell A was a relatively weak rain cell. The defined physical parameters also showed that the mean convective rain rate is 5.52 mm h^{-1} and 17.35 mm h^{-1}, the mean stratiform rain rate 1.16 mm h^{-1} and 2.31 mm h^{-1}, for rain cell A and B, respectively. The defined CAF (convective area fraction to total precipitation area) and SAF (Stratiform area fraction to total precipitation area) are 2.56 %/62.01 % and 97.3 %/37.99 % in rain cell A/B, while CPC (convective precipitation contribution to total precipitation) and SPC (stratiform precipitation contribution to total precipitation) are 11.14 %/92.46 % and 88.79 %/7.54 % in rain cell A/B. This indicates that rain cell B is a convective cell while rain cell A is a stratiform rain cell. Actually, the rain cell B has the maximum reflectivity factor 57.81 dBZ (dBZ_{max}) listed in Table 4 against 36.38 dBZ for rain cell A.

Table 3. The geometric parameters of rain cell A and B calculated by MBR method and BFE method.

~~Rectangle~~MBR method		~~Ellipse~~BFE method	
~~r_L (km)~~ L_r (km)	290.86/169.57	~~e_L (km~~ L_e (km)	347.63/170.66
~~r_W (km)~~ W_r (km)	140.29/76.18	~~e_W (km~~ W_e (km)	139.94/76.76
~~r_α~~ α_r	0.48/0.45	~~e_α~~ α_e	0.4/0.45

~~S_{rain} (km²)~~S_{rain} (km²)	10223.50/4496.40	~~S_{rain} (km²)~~S_{rain} (km²)	10223.50/4496.40
~~r_s (km²)~~S_r (km²)	40803.36/12917.48	~~e_s (km²)~~S_e (km²)	38207.27/10289.43
~~r_β~~ β_r	0.25/0.35	~~e_β~~ β_e	0.27/0.44
H_{max} (km)	8.75/17.75		8.75/17.75
H_{av} (km)	5.59/9.47		5.59/9.47
γ_{max}	0.03/0.11		0.03/0.11
γ_{av}	0.03/0.08		0.03/0.08
H_{avc} (km)	5.76/10.39		5.76/10.39
H_{avs} (km)	5.58/7.96		5.58/7.96
H_dBZ$_{max}$ (km)	3.25/2.75		3.25/2.75
μ	0.37/0.15		0.37/0.15

~~The results of the parameter calculations shown in Table 4 are not affected by the rain cell identification method. For the first case, the H_{max} = 8.75 km, H_{av} = 5.59 km, γ_{max} = 0.03, and γ_{av} = 0.026 show that the vertical scale of the rain cell is at least one order of magnitude smaller than the horizontal scale. The rain cell has RR_{ave} = 1.27 and RR_{max} = 8.08 mm h^{-1}, respectively. The parameters of CAF = 2.6 %, SAF = 97.3 %, CPC = 11% and SPC = 89% indicate that the rain cell is primarily composed of stratiform precipitation. The maximum radar reflectivity factor (dBZ$_{max}$) is 36.38 dBZ, and the relative height (H_dBZ$_{max}$) is 3.25 km. According to the merged data of VIRS and TMI instruments, the $RF1_{ave}$, $TB_{10.8\_ave}$, $TB_{19GHz\_H\_ave}$, $TB_{85GHz\_H\_ave}$ are 0.72, 253.65 K, 260.61 K, and 254.44 K, respectively. These parameters indicate that the stratiform rain cell has less precipitation and weak development.~~

~~**Table 4. The vertical geometric and physical parameters of the first/second case.**~~

Table 4. The physical parameters of rain cell A and B calculated by MBR method and BFE method.

~~Vertical parameter~~			Physical parameter
~~H_{max} (km)~~	~~8.75/17.75~~	RR_{ave} (mm h^{-1})	1.27/11.64
~~H_{av} (km)~~	~~5.59/9.47~~	RR_{max} (mm h^{-1})	8.08/113.14
~~γ_{max}~~	~~0.03/0.11~~	RR_{avc} (mm h^{-1})	5.52/17.35
~~γ_{av}~~	~~0.03/0.08~~	RR_{avs} (mm h^{-1})	1.16/2.31
~~H_{avc} (km)~~	~~5.76/10.39~~	RR_{maxc} (mm h^{-1})	8.08/113.14
~~H_{avs} (km)~~	~~5.58/7.96~~	RR_{maxs} (mm h^{-1})	4.45/11.87
		CAF (%)	~~0.03/0.~~2.56/62.01
		SAF (%)	~~0.~~97/~~0.38~~.3/37.99
		CPC (%)	~~0.~~11/~~0.~~.14/92.46
		SPC (%)	~~0.89/0.08~~88.79/7.54
		dBZ_{max} (dBZ)	36.38/57.81
		~~H_dBZ$_{max}$ (km)~~	~~3.25/2.75~~

设置了格式 … 删除的单元格 … 设置了格式 … 格式化表格 … 设置了格式 … 设置了格式 … 带格式的 … 删除的单元格 … 设置了格式 … 设置了格式 … 设置了格式 … 设置了格式 … 带格式的 … 设置了格式 … 设置了格式 … 设置了格式 … 带格式的 … 设置了格式 … 设置了格式 … 设置了格式 … 设置了格式 … 带格式的 … 设置了格式 … 设置了格式 … 设置了格式 … 设置了格式 … 带格式的 … 设置了格式 … 设置了格式 … 设置了格式 … 带格式的 … 设置了格式 … 设置了格式 … 设置了格式 … 带格式的 … 设置了格式 … 设置了格式 … 设置了格式 … 设置了格式 … 带格式的 … 设置了格式 … 删除的单元格 … 删除的单元格 … 设置了格式 …

For the second case, the H_{max} and H_{av} are 17.75 km and 9.47 km. The parameters γ_{max} = 0.11 and γ_{av} = 0.08 are slightly larger than those in the first case, indicating that the second rain cell is slightly taller than the first one. The parameters RR_{ave} and RR_{max} are 11.64 and 113.14 mm h^{-1} at this rain cell, respectively, which are much larger than those in the first case. In addition, CPC (SPC) in the second case has a value of 92% (8%), larger (smaller) than that in the first case. This indicates that the rain cell in the first case has a greater proportion of stratiform precipitation in the total precipitation (89%), while the second rain cell has a higher proportion of convective precipitation (92%). The parameters dBZ_{max} and H_dBZ_{max} are 57.81 dBZ and 2.75 km, respectively. Compared with the first case, this case has more precipitation and strong convective regions locate in lower layers. Furthermore, $RF1_{ave}$ has a value of 0.69, slightly larger than that in the first case. Except for $TB_{19GHz\_H\_ave}$ = 276.75 K, the $TB_{10.8\_ave}$ = 222.96 K and $TB_{85GHz\_H\_ave}$ = 219.11 K are smaller than the first case. This indicates that the brightness temperature near the cloud top of the rain cell is relatively low, while the convection develops vigorously and there is a higher concentration of ice particles within the cloud.

5.2 Structure of rain cell

In order to further understand the rain cells, the structural distribution of rain cells is given in this section. We also compare the distribution of relevant parameters between the original datasets and the merged datasets. Figure 2 presents the signals detected by the visible, and thermal infrared channels of VIRS onboard TRMM. The solid black line represents the TRMM PR scan track, while the solid red line is the rectangular box of the rain cell. The reflectivity at 0.63 μm is primarily related to cloud optical thickness (COT), and the higher the COT value, the greater the reflectivity. The equivalent brightness temperature of a blackbody at 10.8 μm indicates the height of cloud top, and the higher the cloud top, the lower the brightness temperature of the infrared channel (Luo et al., 2020).

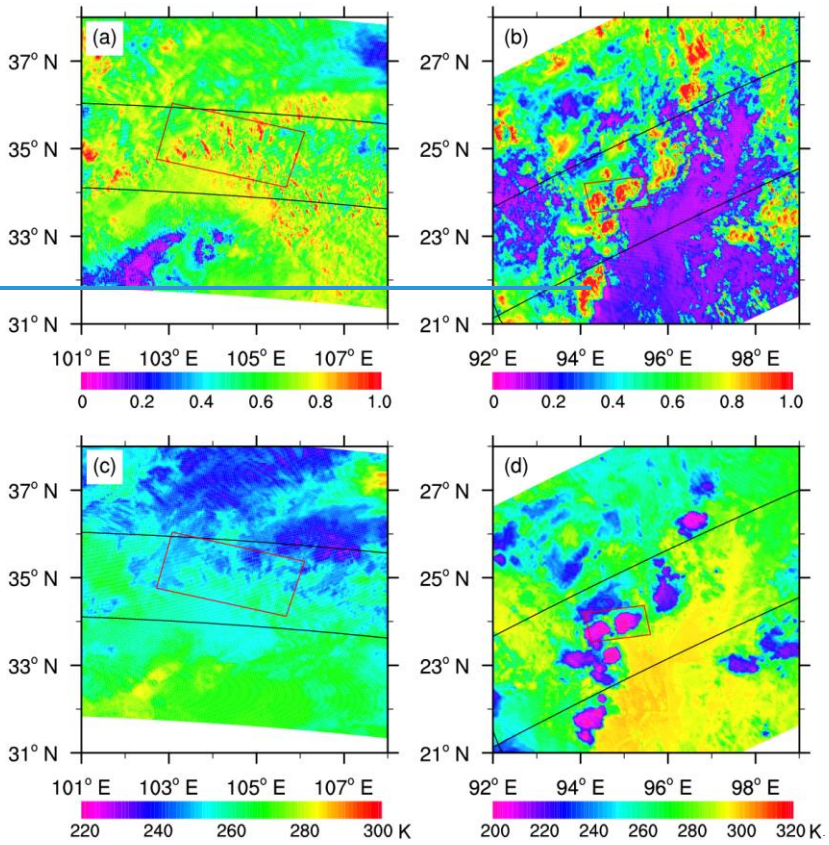

5.2 VIRS and TMI signals of rain cell

Since TRMM PR, VIRS and TMI observed the same target in spatiotemporal synchronization, the spatial distribution of visible reflectivity (0.63 μm) and far-infrared brightness temperature (10.8 μm) for the two rain cells can be given as shown in Figure 2. The figure also shows the rain cell area identified by MBR method and BFE method, which indicates many strips of reflectivity (larger than 0.8) and uniform distribution of brightness temperature (varying from 240 to 250 K) for rain cell A, while rain cell B consists of two convective clouds with reflectivity greater than 0.85 and brightness temperature lower than 220 K. Table 4 also shows the calculated mean visible reflectivity $RF1_{ave}$ for the two rain cells (0.72 and 0.69, respectively). The mean visible reflectivity of convective/stratiform precipitation $RF1_{avc}$/$RF1_{avs}$ for the two rain cells are 0.73/0.72 and 0.66/0.73, respectively. The large reflectivity values indicate that the cloud optical thickness at the top of the two rain cells are large. The mean

brightness temperature at VIRS channel 10.8 μm ($TB_{10.8\_ave}$) shows 253.65 K and 222.96 K for the two rain cells, which indicates that rain cell B has a higher cloud top, i.e. ice phase distributed at cloud top. While the cloud top of rain cell A has ice-liquid mixed phase. The signals of VIRS channels can be used to retrieval cloud parameters. The retrieval algorithms were studied and reviewed by many authors (Nakajima and King, 1990; Rossow and Garder, 1993; Han et al., 1994; Rossow and Schiffer, 1999; Fu, 2014).

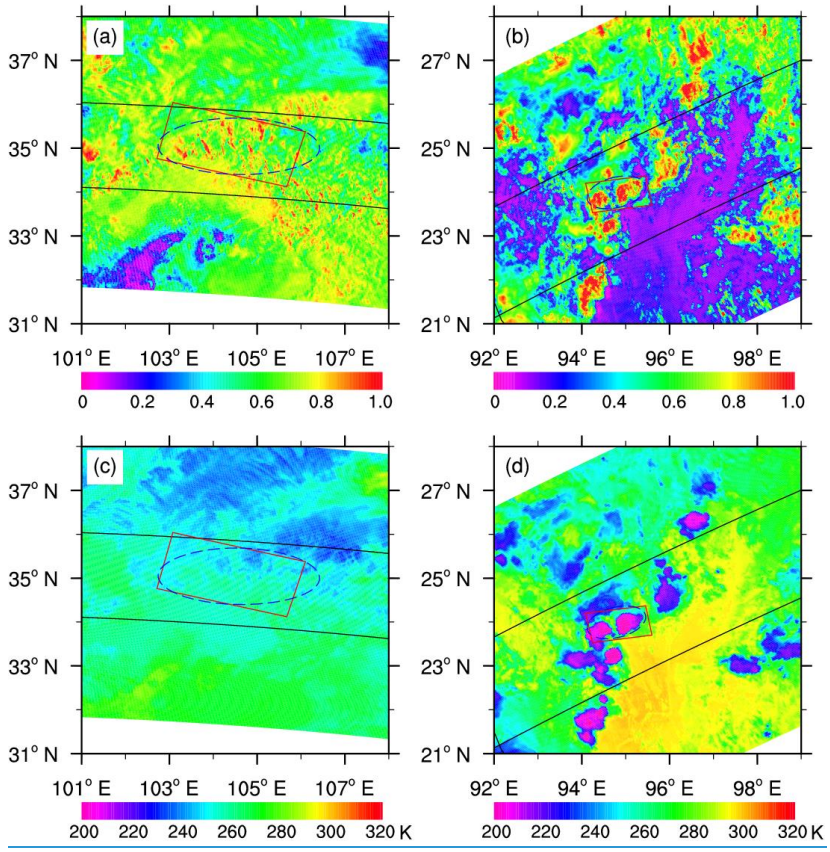

Figure 2. The reflectivity distribution of ~~(a,~~ visible channel at 0.63 μm (a and b) ~~RF1~~ and ~~(c, d) $TB_{10.8}$ for two precipitation cases. The solid black line is the TRMM PR scanning track and the solid red line is the rectangular box of rain cell.~~

~~In Fig. 2a, the reflectance of the visible channel in the rectangular box generally exceeds 0.6, with certain areas exhibiting values above 0.8. This suggests that the COT of certain areas of the stratiform rain cell is large. In addition, the brightness temperature of the 10.8 μm is mainly between 240-260 K~~

~~(Fig. 2c), with low cloud development. There are two central regions with RF1 higher than 0.8 and corresponding $TB_{10.8}$ below 220 K (Figs. 2b, d). This suggests that there are many large-sized and deep ice cloud droplets dominating in the central region of the convective rain cell, with high cloud development. This analysis indicates that the signals obtained by TRMM/VIRS has strong detection ability for the cloud-top structure, and can have a good understanding of the development of the rain cell. According to the theory of microwave remote sensing, the frequency of 10-23 GHz is sensitive to liquid water particles in the cloud, and the frequency of 36-89 GHz is sensitive to liquid and solid particles (ice or snow) in the cloud (Petty, 1994a, 1994b; Fu et al., 2021). Figure 3 shows the~~ **brightness temperature distribution of** ~~the 19 GHz and 85 GHz horizontal polarization channels observed by the TMI. The outline of rain cells cannot be clearly observed for the two cases in Figs. 3a, b, because the emission signal of precipitation particles in the cloud is drowned by the surface emission signal, which is why passive microwave low-frequency signals cannot invert the land surface precipitation (Fu et al., 2021). Figure 3c shows TB_{85GHz_H}, which ranges between 240 and 260 K. The outline of the rain cell can be roughly observed. The TB_{85GHz_H} of two convective central zones in rain cell are around 200-220 K (Fig. 3d), indicating that ice-phase particles are more abundant in the convective precipitation clouds~~**far-infrared channel at 10.8 μm (c and d) for the two cases observed by VIRS (Visible and Infrared Scanner). The solid black line is PR (Precipitation Radar) scanning track. The red solid rectangle and blue dash ellipse represent for the area of rain cell identified by MBR method and BFE method, respectively.**

带格式的: 缩进: 首行缩进: 0 字符, 段落间距段后: 10 磅, 行距: 单倍行距

设置了格式: 字体: 小五, 加粗

设置了格式: 字体: 小五, 加粗

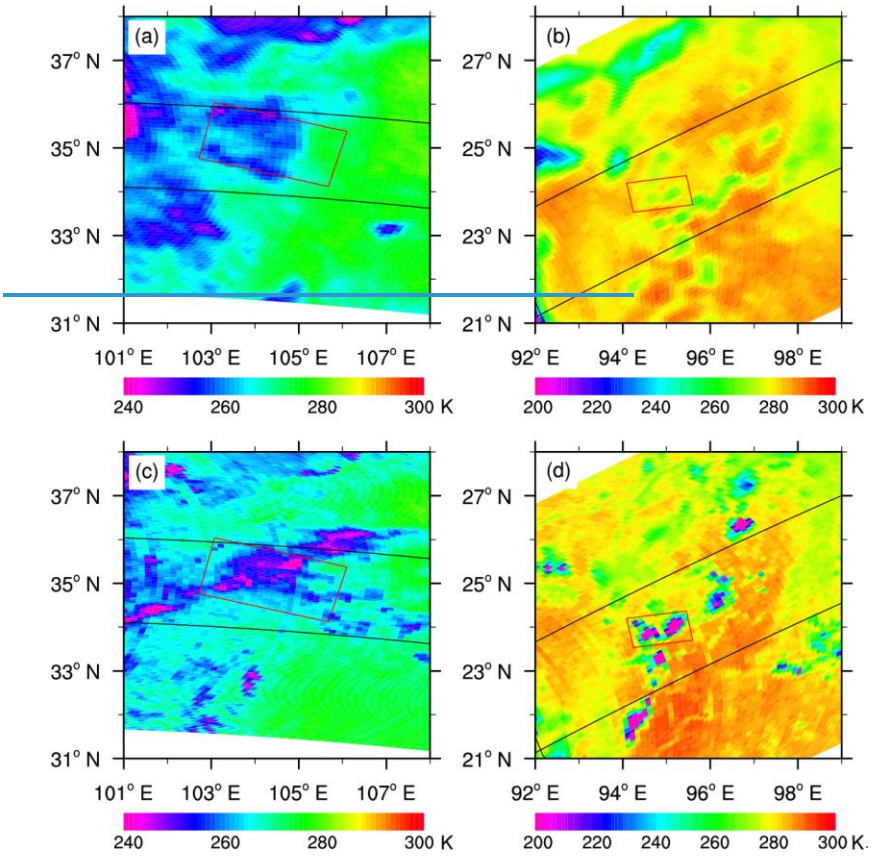

Figure 3. The same as Fig. 2, but for the (a, b) TB_{19GHz_H} and (c, d) TB_{85GHz_H}.

Figure 4 shows the distribution of parameters in the rain cells merged dataset. The stratiform rain cell shown in the first case (Fig. 4a) has a uniform distribution of precipitation, with the maximum rain rate exceeding 4 mm h^{-1}. However, the convective rain cell in the second case (Fig. 4b) presents a non-uniform distribution, with large local variations, and the maximum rain rate can reach more than 20 mm h^{-1}. RF1 in the first case ranges between 0.6 and 0.8 (Fig. 4c). The value in the second case can exceed 0.8 in the area of heavy precipitation, and the corresponding COT is larger (Fig. 4d). $TB_{10.8}$ varies from 240 to 260 K in the first case, and the cloud top height of rain cell is uniformly distributed (Fig. 4e). While the $TB_{10.8}$ in the center of heavy precipitation varies between 200-220 K, which suggests that the cloud top of the center region develops at a high altitude, whereas the altitude of the cloud system around it is relatively low (Fig. 4f). TB_{19GHz_H} for two cases cannot observe valid

~~information due to the surface emissivity. The TB_{85GHz_H} varies uniformly from 240-260 K, which is close to the distribution of the $TB_{10.8}$ (Fig. 4i). The region in the center of the strong precipitation in Fig. 4j is below 200 K, which indicates that the cloud interior contains more ice-phase particles. In a word, the merging process has no dramatic variations on the distribution of original data.~~

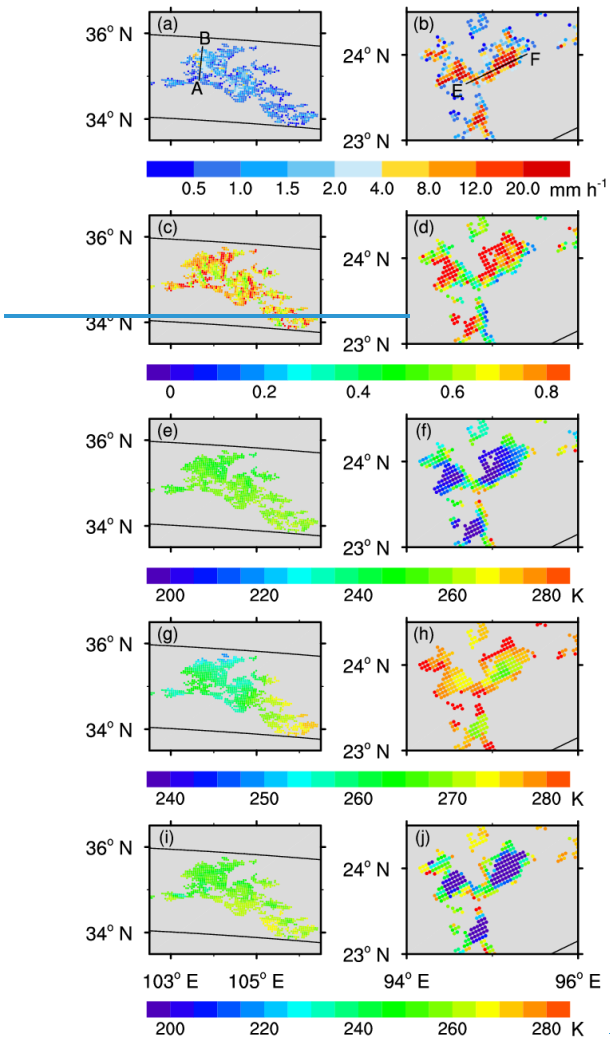

Similar to Figure 2, the distribution of microwave brightness temperature observed by nine channels of TMI can be given. But for simplicity, Figure 3 only plotted the distribution of brightness temperature at TMI horizontal polarization channel 19.4 GHz and 85 GHz. At channel 19.4 GHz, rain cell A shows

relatively lower brightness temperature (from 250 to 280 K), rain cell B has higher brightness temperature (from 260 to 290 K). Because the low-frequency microwave channel is easily affected by the radiation on land surface, it can be judged that the temperature of land surface in rain cell A is lower than that in rain cell B. The brightness temperature of microwave high frequency channels is mainly affected by the composition of ice phase inside cloud, such as ice particles and supercooled water, while the influence of land surface radiation on these channels is weak. The more content of ice phase composition inside cloud, the lower brightness temperature at these high frequency channels. According to this principle, rain cell B shows low brightness temperature at 85 GHz in Figure 3d because the rain cell belongs to deep convective precipitation system. While rain cell A has more stratiform precipitation and less ice particles, so the brightness temperature at this same channel is higher. In Table 4, the mean brightness temperature at channel 19.4 GHz and 85 GHz also indicates the difference between the two rain cells, and the difference between the two rain types. The microwave brightness temperature of TMI channels can be used to retrieval cloud parameters such as ice water or liquid water or rain rate based on retrieval algorithms of previous studies (Grody, 1976; Grody et al., 1980; Liu and Curry, 1993; Petty, 1994a, 1994b; Wang et al., 2009; Fu, 2021).

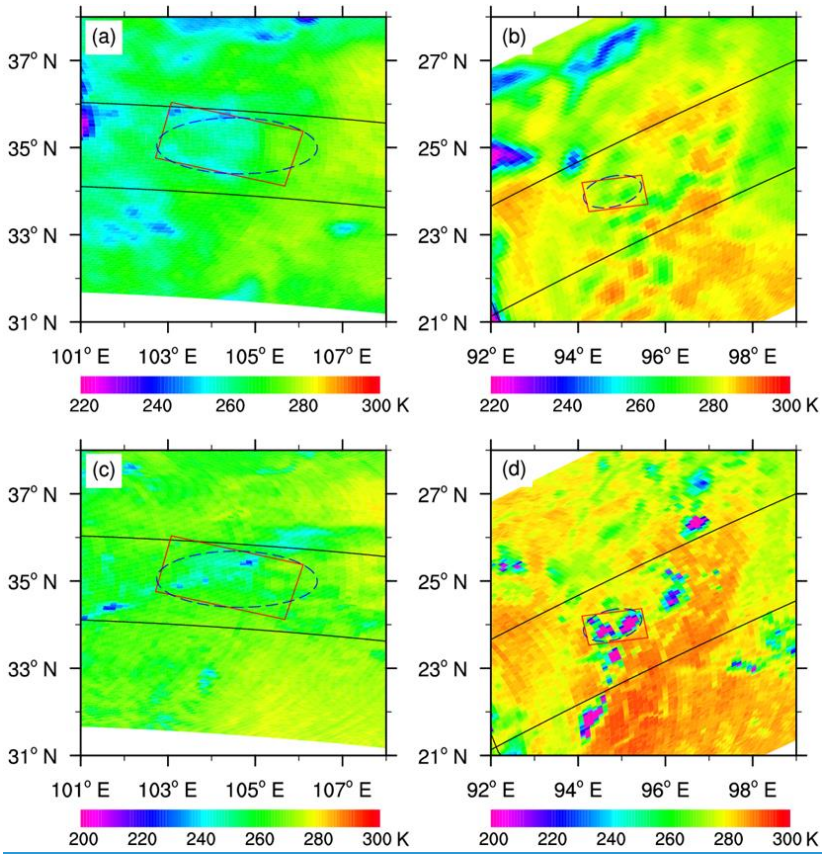

Figure 3. The brightness temperature distribution of microwave horizontal polarization channel at 19 GHz (a and b) and at 85 GHz (c and d) for the two cases observed by TMI (TRMM Microwave Imager). The solid black line is PR (Precipitation Radar) scanning track. The red solid rectangle and blue dash ellipse represent for the area of rain cell identified by MBR method and BFE method, respectively.

In order to visually display the parameter distribution of rain cell A and B identified by MBR method and BFE method, Figure 4 shows the distribution of rain rate, reflectivity at VIRS visible channel, brightness temperature at VIRS thermal infrared channel, microwave brightness temperature at TMI low frequency and high frequency channel. It must be pointed out that both VIRS and TMI signals in Figure 4 correspond to PR precipitation pixels (that is, signals corresponding to each resolution of PR pixel), and these signals are not given if there is no precipitation area in the rain cell. Therefore, the rain cell data established in this study facilitate the study of relationship among precipitation, visible/infrared and microwave signals.

A simple application is shown in Figure 5, which displays the multi-parameter distribution along the AB line and EF line in Figure 4a and 4b, respectively. The vertical cross sections of reflectivity factor (Figure 5a and 5b) show that rain cell A is shallow and weak precipitation, while rain cell B is deep convective precipitation. The strong echo (greater than 38 dBZ) of rain cell B displays higher, near to 16 km. The visible reflectivity (Figure 5c and 5d) from the cloud tops of the two rain cells varies between 0.4 and 0.8, and the reflectivity of the strong echo region in rain cell B is higher (greater than 0.6). The near infrared reflectivity (Figure 5c and 5d) varies from 0.1 to 0.4, which means there are a lot of ice particles inside cloud for the two rain cells. The infrared brightness temperature at VIRS channel 3.7 μm (Figure 5e and 5f) shows higher in rain cell A, relatively lower in rain cell B, which indicates the difference between the two rain cells. At VIRS channel 10.8 μm and 12.0 μm, rain cell A has uniform brightness temperature, one of the characteristics of cloud top for stratiform precipitation system, while rain cell B appears the characteristics of deep convective cloud top, high cloud top with low brightness temperature. For the four horizontal polarization channels of TMI (Figure 5i and 5j), the microwave brightness temperature of rain cell A is uniformly distributed, and the brightness temperature of each channel has little difference. In rain cell B, the brightness temperature at low-frequency channel, 10 GHz and 19 GHz, is also evenly distributed, and the brightness temperature at the two channels is higher than that in rain cell A, but the brightness temperature at channel 37 GHz and 85 GHz changes significantly. Corresponding to the strong echo region in Figure 5b, the brightness temperature of the two channels is low, indicating that there are more ice particles inside cloud in strong echo region of rain cell B. The above indicates that the established new data can be used to analyze the corresponding spectral and microwave characteristics of precipitating clouds.

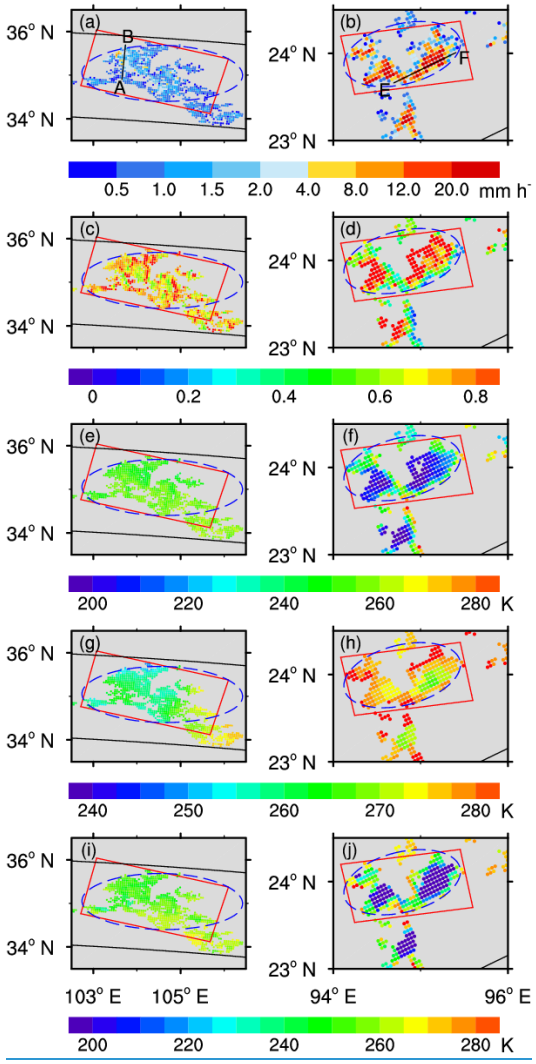

Figure 4. The distributions of ~~(a, b) the~~ near-surface rain rate~~,~~ (a and b), reflectivity at channel 0.63 μm (c~~,~~ and d~~) RF1,~~), brightness temperature at far-infrared channel 10.8 μm (e~~,~~ and f~~) $TB_{10.8,}$~~), brightness temperature at horizontal channel 19 GHz (g~~, h) $TB_{19GHz,H,}$~~ and h) and at 85 GHz (i~~,~~ and j) ~~$TB_{85GHz,H}$~~ for the two ~~precipitation~~ cases based on the merged ~~datasets~~data.

~~The distribution of radar reflectivity factor along the AB (as shown in the Fig. 4a) profile in Fig. 5a reveals that stratiform precipitation does not extend vertically beyond 8 km, with some areas exhibiting stratification. A shallow bright band is observed at a height of 4 km. The radar reflectivity factor of the~~

带格式的: 段落间距段后: 10 磅

~~precipitation is generally below 32 dBZ, indicating weak precipitation activity. Figure 5c shows that the reflectivity of the 0.63 μm channel varies mainly between 0.5 and 0.8. The 1.6 μm channel varies between 0.1 and 0.3, with these low signal levels further suggesting the presence of numerous ice-phase regions. The change in the brightness temperature profile shows that the top of the stratiform precipitation cloud has a higher temperature and correspondingly lower cloud top height (Fig. 5e). The microwave brightness temperature values vary uniformly between 250 and 270 K, which may be strongly influenced by the surface emissivity and thus may not serve as an accurate indicator (Fig. 5i).~~

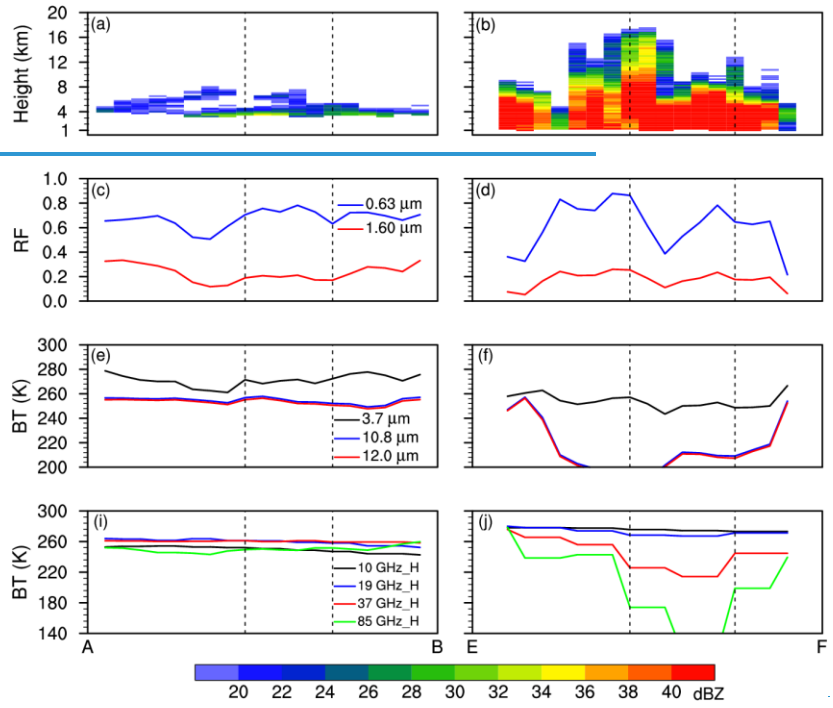

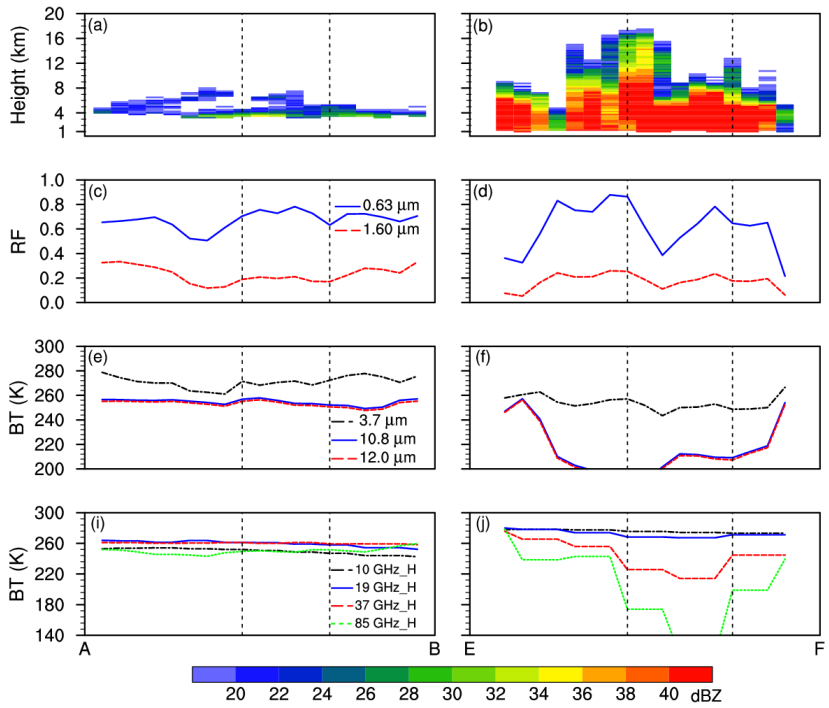

Figure 5. The vertical cross sections of ~~(a, b) the radar~~ reflectivity factor~~,~~ (a and b), reflectivity at VIRS channel 0.63 μm and 1.60 μm (c~~, d) reflectivity, (e, and d), infrared brightness temperature at VIRS channel 3.7 μm, 10.8 μm and 12.0 μm (e and f) infrared brightness temperatures, (i, j)),~~ microwave brightness temperature at TMI horizontal channel 10 GHz, 19 GHz, 37 GHz and 85 GHz along ~~the A-B~~AB line and ~~E-F~~EF line as shown in ~~Fig 4~~Figure 4a and 4b.

~~Figure 5b shows that the radar reflectivity factor presents an uneven distribution in both vertical and horizontal directions due to the irregular movement of precipitation particles in the precipitation cloud with the airflow. The echo top height can reach up to 17 km, which also means that strong convection occurs here. In addition, the radar reflectivity factor of near surface exceeds 38 dBZ, indicating heavy precipitation near the surface. RF1 varies from 0.3 to 0.9, which means that the COT is unevenly distributed. RF2 does not vary strongly, suggesting that the phase distribution in the cloud is uniform and mostly ice-phase particles (Fig. 5d). The brightness temperature of far-infrared in the region of strong convective development is lower than the other locations (Fig. 5f). Meanwhile, the height of the cloud top is higher in the corresponding region. TB_{10GHz_H} and TB_{19GHz_H} vary uniformly and does not respond well to precipitation. The low value area of the TB_{37GHz_H} and TB_{85GHz_H} tend to correspond~~

带格式的: 段落间距段后: 10 磅

~~well to areas of strong precipitation, as shown by the location of the dotted dashes in Fig. 5j. There are often filled with a high concentration of ice-phase particles in the areas of strong precipitation, leading to strong scattering signal.~~

6 Data availability

The rain cell ~~precipitation parameters~~ dataset based on identification methods of MBR and BFE together with defined geometric and physical parameters to describe rain cell characteristics used in this study is accessible at https://doi.org/10.5281/zenodo.13118878.

7 Conclusions

In order to study the characteristics of geometric and physical parameters of rain cell, the basic unit in natural precipitation system, this study was inspired by earlier studies and made full use of the advantages of TRMM PR, VIRS and TMI observations, i.e. the precipitation profile of PR reflecting precipitation structure, the visible~~/~~ and infrared ~~and~~ signals of VIRS representing cloud top information, and the microwave ~~signal datasets used in this paper are accessible at https://doi.org/10.5281/zenodo.8352587~~signals of TMI reflecting hydrometeors in cloud columns. By matching and merging these data at PR pixels, the minimum bounding rectangle (MBR) method and the best fit ellipse (BFE) method were used to identify rain cell within PR scanning width, and the geometric and physical parameters of the rain cell were defined, thus a new rain cell data was established.

~~7 Discussion and conclusions~~

~~We establish a new rain cell precipitation parameter and visible-infrared and microwave signal dataset combining with the multi-instrument observation data on TRMM. PR provides the three-dimensional precipitation structure of the rain cell, VIRS provides the spectral signal of the top of the rain cell, and TMI provides the phase information of the particles inside the rain cell. The purpose of~~ In this ~~dataset is to promote the three-dimensional~~ study ~~of rain cell precipitation system, and reveal the spatial and temporal variations of the scale morphology and intensity of the system.~~

~~First, we compare the difference between the MBR rain cell identification method and the BFE rain~~

设置了格式: 字体: 10 磅, 加粗, 字体颜色: 自动设置

带格式的: 1 级, 段落间距段前: 24 磅, 段后: 12 磅

~~cell identification method in describing rain cell shape. The two methods are mainly different in ,~~ the geometric parameters ~~such as L, W, α, S, and β. According to the parameter calculation results, both methods can reflect the geometric characteristics of rain cells effectively. Compared with the MBR method, the BFE method can obtain the fitting result of the smallest rain cell area and its β value is correspondingly larger than that of the MBR method. However, we adopt the MBR method to identify rain cells in the new dataset because it can simplify the data storage volume.~~

~~Second, we calculate other parameters of two types of rain cell, including vertical geometric parameters (average cloud top~~(length, width, height~~, horizontal scale, spatial morphology,~~ and so on) and physical parameters (~~average~~ rain rate, ~~maximum~~visible reflectivity ~~factor and its corresponding height, average visible reflectivity, average~~ and thermal infrared brightness temperature~~, and so on). The statistical results show that the defined parameters can effectively reflect the three-dimensional morphology of rain cells and the development state of precipitation system, which can provide reference for exploration of the relationship between rain cell morphology parameters and precipitation.~~

~~Third, we use the new dataset to analyze the distribution of precipitation parameters,~~ from cloud top, and microwave brightness temperature from cloud ~~top radiation signal, and brightness temperatures and the profile characteristics of two rain cells. The study shows that merged dataset can significantly display the features of the original dataset. For the stratiform rain cell, the rain rate is relatively small, with high cloud top brightness temperature, low cloud top height, and~~ column) of the two rain cells (weak ~~vertical movement. For the~~rain cell and strong rain cell) identified by MBR method and BFE method are calculated. The results show that the weak rain cell shows stratiform precipitation with small rain rate, while the strong rain cell exhibits convective ~~rain cell, the rain rate is large and the distribution is uneven with low cloud top brightness~~precipitation with deep in vertical direction and also has low thermal infrared bright temperature~~, high cloud top height, and strong vertical movement. The difference of parameter distribution between two types of rain cells is obvious, which lays a foundation for the subsequent study on the characteristics of precipitation~~ in cloud top. All these indicate that the both MBR method and BFE method for rain cell identification, and the defined rain cell parameters are reasonable and intuitive.

~~To further explore the characteristics of rain cell, the cloud parameters based on the signal retrieval from the TRMM VIRS data and the latent heat of precipitation inside the rain cell will be added to the~~

~~dataset. This work is currently in progress but will not be covered in this study due to the limited length of the paper. The dataset will support the research on the development mechanism of precipitation system and promote the progress of precipitation model simulation in the future. With the continuous development of satellite technology, the dataset will add longer time scale data and more effective parameters.~~

It must be noted that the difference between MBR method and BFE method is only in the horizontal geometric parameters of the rain cell, and the difference is not large, such as the slight difference in length and width of the rain cell, but the vertical geometric parameters of the rain cell are not affected. The physical parameters of the rain cell are not affected by the identification method.

The new rain cell data in this study can be used to study the characteristics of rain cell geometric and physical parameters. Although a lot of achievements have been made in this aspect, systematic and in-depth analysis is still needed, such as the regional differences of these parameters and the characteristics of climate change. It can also be used to analyze the relationship between the physical and geometric parameters of rain cell, which also have regional differences. The effective radius of cloud particles, optical thickness, liquid water path and other parameters in rain cell can be obtained by combining retrieval algorithms of visible and near infrared reflectivity, which can analyze the characteristics of cloud physical parameters of rain cell. These parameters such as cloud water and ice water in column, cloud temperature and rain rate in rain cell can also be obtained by using microwave brightness temperature retrieval algorithms, and the relationship among these parameters can be analyzed. It is believed that the previously mentioned studies will produce results shortly.

Author contribution. ZW and YF prepared the data in the standardized format. ZW uploaded the data in the data repository and prepared the manuscript with contribution from YF. All the authors discussed the concepts and edited the manuscript.

Competing interests. The authors declare that they have no conflict of interest.

Acknowledgements. We would like to acknowledge the National Aeronautics and Space Administration (NASA) for providing TRMM PR, VIRS and TMI datasets.

设置了格式: 字体颜色: 红色

设置了格式: 字体: 10 磅, 加粗, 字体颜色: 自动设置

设置了格式: 字体颜色: 自动设置

带格式的: 行距: 1.5 倍行距

设置了格式: 字体: 10 磅, 加粗, 字体颜色: 自动设置

设置了格式: 字体: 10 磅, 加粗, 字体颜色: 自动设置

设置了格式: 字体: 10 磅, 加粗

Financial support. This research has been supported by the National Natural Science Foundation of China (grant nos. 42230612 and 42275140~~).~~) and The Second Tibetan Plateau Scientific Expedition and Research (STEP) program (grant no. 2019QZKK0104)

~~Review statement.~~

References

Austin, P. M. and Houze, R. A.: Analysis of the structure of precipitation patterns in New England, J. Appl. Meteorol., 11, 926–935, https://doi.org/10.1175/1520-0450(1972)011<0926:Aotsop>2.0.Co;2, 1972.

Awaka, J.: A three-dimensional rain cell model for the study of interference due to hydrometeor scattering, J. Commun. Res. Lab., 36, 13–44, 1989.

Awaka, J., Iguchi, T., Kumagai, H., and Okamoto, K.: Rain type classification algorithm for TRMM precipitation radar, IEEE International Geoscience and Remote Sensing Symposium Proceedings. Remote Sensing – A Scientific Vision for Sustainable Development, Singapore, 3–8 August 1997, https://doi.org/10.1109/IGARSS.1997.608993, 1997.

~~Bacchi, B., Ranzi, R., and Borga, M.: Statistical characterization of spatial patterns of rainfall cells in extratropical cyclones, J. Geophys. Res. Atmos., 101, 26277-26286, https://doi.org/10.1029/96jd01381, 1996.~~

Begum, S. and Otung, I. E.: Rain cell size distribution inferred from rain gauge and radar data in the UK, Radio. Sci., 44, RS2015, https://doi.org/10.1029/2008RS003984, 2009.

Cai, H. K., Mao, Y. Q., Zhu, X. H., Fu, Y. F., and Zhou, R. J.: Comparison of the minimum bounding rectangle and minimum circumscribed ellipse of rain cells from TRMM, Adv. Atmos. Sci., 41, 484–499, https://doi.org/10.1007/s00376-023-2281-9, 2024.

Capsoni, C., Fedi, F., Magistroni, C., Paraboni, A., and Pawlina, A.: Data and theory for a new model of the horizontal structure of rain cells for propagation applications, Radio. Sci., 22, 395–404, https://doi.org/10.1029/RS022i003p00395, 1987.

设置了格式: 字体: 10 磅, 加粗, 字体颜色: 自动设置
设置了格式: 字体: 10 磅, 加粗
设置了格式: 字体: (默认) 宋体, 10 磅
带格式的: 行距: 1.5 倍行距
设置了格式: 字体: 10 磅, 加粗, 字体颜色: 自动设置
带格式的: 1 级, 段落间距段前: 24 磅, 段后: 12 磅
设置了格式: 字体: 10 磅
带格式的: 行距: 1.5 倍行距
设置了格式: 字体: 10 磅
设置了格式: 字体: 10 磅
设置了格式: 字体: 10 磅
设置了格式: 字体: 10 磅
带格式的: 行距: 1.5 倍行距
设置了格式: 字体: 10 磅
设置了格式: 字体: 10 磅
带格式的: 行距: 1.5 倍行距
设置了格式: 字体: 10 磅

Chen, Y. L., Zhang, A. Q., Fu, Y. F., Chen, S. M., and Li, W. B.: Morphological characteristics of precipitation areas over the Tibetan Plateau measured by TRMM PR, Adv. Atmos. Sci., 38(4), 677–689, https://doi.org/10.1007/s00376-020-0233-1, 2021.

~~Durden, S. L., Im, E., Haddad, Z. S., and Li, L.: Comparison of TRMM precipitation radar and airborne radar data, J.~~ Han, Q., Rossow, W. B., and Lacis, A. A.: Near-global survey of effective droplet radii in liquid water clouds using ISCCP data, J. Climate, 7, 465–497, https://doi.org/10.1175/1520-0442(1994)007<0465:NGSOED>2.0.CO;2, 1994.

~~Appl. Meteorol., 42, 769-774, https://doi.org/10.1175/1520-0450(2003)042<0769:Cotpra>2.0.Co;2, 2003.~~

Feral, L., Mesnard, F., Sauvageot, H., Castanets, L., and Lemorton, J.: Rain cells shape and orientation distribution in south-west of France, Phys. Chem. Earth B: Hydrol. Oceans Atmos., 25, 1073–1078, https://doi.org/10.1016/s1464-1909(00)00155-6, 2000.

Fu, Y. F.: Cloud ~~Parameyers~~parameyers retrieved by the bispectral reflectance algorithm and associated applications, J. Meteorol. Res-Prc., 28, 965–982, https://doi.org/10.1007/s13351-014-3292-3, 2014. (in Chinese).

Fu, Y. F.: Research progress on retrieval algorithms of cloud liquid water over ocean based on remote sensing by satellite-borne passive microwave instruments, Torrential Rain and Disasters, 40, 217–230, https://doi.org/10.3969/j.issn.1004-9045.2021.03.001, 2021 (in Chinese).

Fu, Y. F., Chen, Y., Zhang, X., Wang, Y., Li, R., Liu, Q., Zhong, L., Zhang, Q., and Zhang, A.: Fundamental characteristics of tropical rain cell structures as measured by TRMM PR, J. Meteorol. Res-Prc., 34, 1129–1150, https://doi.org/10.1007/s13351-020-0035-5, 2020.

~~Fu, Y. F., Liu, D., Wang, Y., Yu, R. C., Xu, Y. P., Cheng, R.: Characteristics of precipitating and non-precipitating clouds in typhoon RANAN as viewed by TRMM combined measurements, Acta Meteorologica Sinica, 65, 316-328, https://doi.org/10.3321/j.issn:0577-6619.2007.03.002, 2007a (in Chinese).~~

Fu, Y. F. and Liu, G. S.: The variability of tropical precipitation profiles and its impact on microwave brightness temperatures as inferred from TRMM data, J. Appl. Meteorol., 40, 2130–2143, https://doi.org/10.1175/1520-0450(2001)040<2130:Tvotpp>2.0.Co;2, 2001.

~~Fu, Y. F., Liu, Q., Gao, Y., Hong, X. Y., Zi, Y., Zheng, Y. Y., Li, R., and Heng, Z. W.: A feasible method for merging the TRMM microwave imager and precipitation radar data, J. Quant. Spectrosc. Ra., 122, 155-169, https://doi.org/10.1016/j.jqsrt.2012.08.028, 2013.~~

Fu, Y. F., Liu, P., Liu, Q., Ma, M., Sun, L., and Wang, Y.: Climatological Characteristics of VIRS

设置了格式: 字体: 10 磅
带格式的: 行距: 1.5 倍行距

Channels for Precipitating Cloud in Summer Over the Tropics and Subtropics, J. Atmos. Environ. Optics., 6, 129–140, https://doi.org/10.3969/j.issn.1673- 6141.2011.02.009, 2011 (in Chinese).

Gagin, A., Rosenfeld, D., Woodley, W. L., and Lopez, R. E.: 1986: Results of seeding for dynamic effects on rain-cell properties in FACE-2, J. Appl. Fu, Y. F., Luo, J., Luo, S., Chen, G. C., Wang, M. X., Sun, L. L., Sun, N., and Yang, L.: Rainstorm structure of a supercell cloud occurred in Chongqing in May 2018 measured by GPM DPR and GMI, Torrential Rain and Disasters, 41, 1-14, https://doi.org/10.3969/j.issn.1004-9045.2022.01.001, 2021 (in Chinese).

Fu, Y. F., Yu, R. C., Cui, C. G., Xu, Y. P., Meteor. Climatol., 25, 3–13, https://doi.org/10.1175/1520-0450(1986)025<0003:ROSFDE>2.0.CO;2, 1986.

Liu, G. S., Liu, Y., Zheng, Y. Y.: The structure characteristics of precipitating clouds over the east Asia based on TRMM Measurements, Torrential Rain and Disasters, 26, 9-20, https://doi.org/10.3969/j.issn.1004-9045.2007.01.003, 2007b (in Chinese).

Goldhirsh, J. and Musiani, B.: Rain cell size statistics derived from radar observations at Wallops Island, Virginia, IEEE TransT. Geosci. Remote Sens., GE-24, 947–954, https://doi.org/10.1109/TGRS.1986.289711, 1986.

Grody, N. C.: Remote sensing of atmospheric water content from satellites using microwave radiometry, IEEE T. Antenn. Propag., 24, 155–162, https://doi.org/10.1109/TAP.1976.1141324, 1976.

Grody, N. C., Grubel, A., and Shen, W. C.: Atmospheric water content over the tropical Pacific derived from the Nimbus-6 scanning microwave spectrometer, J. Appl. Meteor., 19, 986–996, https://doi.org/10.1175/1520-0450(1980)019<0986:AWCOTT>2.0.CO;2, 1980.

He, H. Z., Cheng, M. H., and Zhou, F. X.: 3D structure of rain and cloud hydrometeors for Typhoon Kujira (0302), Chinese Journal of Atmospheric Sciences,J. Atmos. Sci., 30, 491–503, https://doi.org/10.3878/j.issn.1006-9895.2006.03.12, 2006 (in Chinese).

Houze, R. A.: Structures of atmospheric precipitation systems: A global survey, Radio. Sci., 16, 671–689, https://doi.org/10.1029/RS016i005p00671, 1981.

Houze, R. A.: Stratiform Precipitation in Regions of Convection: A Meteorological Paradox?, B. Am. Meteorol. Soc., 78, 2179–2196, https://doi.org/10.1175/1520- 0477(1997)078<2179:SPIROC>2.0.CO;2, 1997.

Houze, R. A., Jr., Rasmussen, K. L., Zuluaga, M. D., and Brodzik, S. R.: The variable nature of convection in the tropics and subtropics: A legacy of 16 years of the Tropical Rainfall Measuring Mission satellite, Rev Geophys, 53, 994-1021, https://doi.org/10.1002/2015RG000488, 2015.

Konrad, T. G.: Statistical models of summer rainshowers derived from fine-scale radar observations, J. Appl. Meteorol., 17, 171–188, https://doi.org/10.1175/1520-0450(1978)017<0171:SMOSRD>2.0.Co;2,

设置了格式: 字体: 10 磅
设置了格式: 字体: 10 磅
设置了格式: 字体: 10 磅
设置了格式: 字体: 10 磅
带格式的: 行距: 1.5 倍行距
设置了格式: 字体: 10 磅
设置了格式: 字体: 10 磅
设置了格式: 字体: 10 磅
设置了格式: 字体: 10 磅
带格式的: 行距: 1.5 倍行距
设置了格式: 字体: 10 磅
设置了格式: 字体: 10 磅
设置了格式: 字体: Times New Roman, 10 磅
设置了格式: 字体: 10 磅
设置了格式: 字体: 10 磅
设置了格式: 字体: 10 磅
带格式的: 行距: 1.5 倍行距
设置了格式: 字体: 10 磅

1978.

Kozu, T., Kawanishi, T., Kuroiwa, H., Oikawa, M., Kumagai, H., Okamoto, K., Okumura, M., Nakatsuka, H., and Nishikawa, K.: Development of precipitation radar onboard the Tropical Rainfall Measuring Mission (TRMM) satellite., IEEE T. Geosci. Remote. Sens., 39, 102–116, https://doi.org/10.1109/36.898669, 2001.

Kummerow, C., Barnes, W., Kozu, T., Shiue, J., and Simpson, J.: The Tropical Rainfall Measuring Mission (TRMM) Sensor Package, J. Atmos. Ocean. Tech., 15, 809–817, https://doi.org/10.1175/1520-0426(1998)015<0809:TTRMMT>2.0.Co;2, 1998.

Kummerow, C., Simpson, J., Thiele, O., Barnes, W., Chang, A. T. C., Stocker, E., Adler, R. F., Hou, A., Kakar, R., Wentz, F., Ashcroft, P., Kozu, T., Hong, Y., Okamoto, K., Iguchi, T., Kuroiwa, H., Im, E., Haddad, Z., Huffman, G., Ferrier, B., Olson, W. S., Zipser, E., Smith, E. A., Wilheit, T. T., North, G., Krishnamurti, T., and Nakamura, K.: The Status of the Tropical Rainfall Measuring Mission (TRMM) after two years in orbit, J. Appl. Meteorol. Climatol., 39, 1965–1982, https://doi.org/10.1175/1520-0450(2001)040<1965:Tsottr>2.0.Co;2, 2000.

Lau, K. M. and Wu, H. T.: Characteristics of ~~Precipitation, Cloud~~precipitation, cloud, and ~~Latent Heating Associated~~latent heating associated with the Madden-Julian ~~Oscillation~~oscillation, J. Climate, 23, 504–518, https://doi.org/10.1175/2009jcli2920.1, 2010.

Li, R. and Fu, Y. F.: Tropical precipitation estimated by GPCP and TRMM PR observations, Adv. Atmos. Sci., 22, 852–864, https://doi.org/10.1007/BF02918685, 2005.

~~Liu, C. T. and Zipser, E.~~Liu, C. T., Zipser, E. J., and Nesbitt, S. W.: Global distribution of tropical deep convection: different perspectives from TRMM infrared and radar data, J. Climate, 20, 489–503, https://doi.org/10.1175/JCLI4023.1, 2007.

~~: Regional variation of morphology of organized convection in the tropics and subtropics, J. Geophys. Res. Atmos., 118, 453-466, https://doi.org/10.1029/2012JD018409, 2013.~~

Liu, C. T., Zipser, E. J., Cecil, D. J., Nesbitt, S. W., and Sherwood, S.: A cloud and precipitation feature database from nine years of TRMM observations, J. Appl. Meteorol. Climatol., 47, 2712–2728, https://doi.org/10.1175/2008jamc1890.1, 2008.

Liu, C. T. and Zipser, E. J.: Regional variation of morphology of organized convection in the tropics and subtropics, J. Geophys. Res~~: "Warm Rain" in the tropics: Seasonal and regional distributions based on 9 yr of TRMM data, J. Climate, 22, 767-779.~~ Atmos., 118, 453–466,

设置了格式: 字体: Times New Roman, 10 磅
设置了格式: 字体: 10 磅
设置了格式: 字体: 10 磅
设置了格式: 字体: 10 磅
设置了格式: 字体: 10 磅
设置了格式: 字体: 10 磅
设置了格式: 字体: 10 磅
设置了格式: 字体: 10 磅
设置了格式: 字体: 10 磅
设置了格式: 字体: 10 磅
设置了格式: 字体: 10 磅
设置了格式: 字体: 10 磅
带格式的: 行距: 1.5 倍行距
设置了格式: 字体: 10 磅
设置了格式: 字体: 10 磅

https://doi.org/10.1029/2012JD018409, 2013.

Liu, G. S. and Curry, J. A.: Determination of characteristic features of cloud liquid water from satellite microwave measurements, J. Geophys. ~~1175/2008jcli2641.1, 2009~~Res., 98, 5069–5092, https://doi.org/10.1029/92JD02888, 1993.

Liu, G. S. and Fu, Y. F.: The characteristics of tropical precipitation profiles as inferred from satellite radar measurements, J. Meteor. Soc. Japan, 79, 131–143, https://doi.org/10.2151/jmsj.79.131, 2001.

Liu, Q. and Fu, Y. F.: Comparison of radiative signals between precipitating and non-precipitating clouds in frontal and typhoon domains over East Asia, Atmos. Res., 96, 436–446, https://doi.org/10.1016/j.atmosres.2010.02.003, 2010.

Nakajima, T. and King, M. D.: Determination of the optical thickness and effective particle radius of clouds from reflected solar radiation measurements. Part I: Theory, J. Atmos. Sci., 47, 1878–1893, https://doi.org/10.1175/1520-0469(1990)047<1878:DOTOTA>2.0.CO;2, 1990.

Nesbitt, S. W., Cifelli, R., and Rutledge, S. A.: Storm morphology and rainfall characteristics of TRMM precipitation features, Mon. Wea. Rev., 134, 2702~~Luo, S., Fu, Y. F., Zhou, S. N., Wang, X. F., and Wang, D. Y.: Analysis of the relationship between the cloud water path and precipitation intensity of mature typhoons in the northwest Pacific ocean, Adv. Atmos. Sci, 37, 359-376, https://doi.org/10.1007/s00376-020-9204-9, 2020.~~
–2721, https://doi.org/10.1175/MWR3200.1, 2006.

Nesbitt, S. W., Zipser, E. J., and Cecil, D. J.: A census of precipitation features in the tropics using TRMM: Radar, ice scattering, and lightning observations, J. Climate, 13, 4087–4106, https://doi.org/10.1175/1520-0442(2000)013<4087:ACOPFI>2.0.Co;2, 2000.

Ni, X., Liu, C., Zhang, Q., and Cecil, D. J.: Properties of hail storms over China and the United States from the Tropical Rainfall Measuring Mission, J. Geophys. Res.-Atmos., 121, 12031–12044, https://doi.org/10.1002/2016JD025600, 2016.

~~Nesbitt, S. W., Zipser, E. J., and Cecil, D. J.: A census of precipitation features in the tropics using TRMM Radar, ice scattering, and lightning observations, J. Climate, 13, 4087-4106, https://doi.org/10.1175/1520-0442(2000)013<4087:ACOPFI>2.0.CO;2, 1999.~~

Oki, T. and Kanae, S.: Global hydrological cycles and world water resources, Science, 313, 1068–1072, https://doi.org/10.1126/science.1128845, 2006.

Petty, G.W.: Physical retrievals of over-ocean rain rate from multichannel microwave imagery. Part I: Theoretical characteristics of normalized polarization and scattering indices, Meteorl. Atmos. Phys., 54, 79–99, https://doi.org/10.1007/BF01030053, 1994a.

设置了格式: 字体: 10 磅
带格式的: 行距: 1.5 倍行距
设置了格式: 字体: 10 磅
设置了格式: 字体: 10 磅
设置了格式: 字体: 10 磅
设置了格式: 字体: 10 磅
设置了格式: 字体: 10 磅
设置了格式: 字体: 10 磅
带格式的: 行距: 1.5 倍行距
设置了格式: 字体: 10 磅
设置了格式: 字体: 10 磅
设置了格式: 字体: 10 磅
设置了格式: 字体: 10 磅
带格式的: 行距: 1.5 倍行距

Petty, G.W.: Physical retrievals of over-ocean rain rate from multichannel microwave imagery. Part II: Algorithm implementation, Meteorl. Atmos. Phys., 54, 101–121, https://doi.org/10.1007/BF01030054, 1994b.

~~Rutledge, S. A., Cifelli, R., and Nesbitt, S. W~~Rossow, W. B. and Garder, L. C.: Cloud detection using satellite measurements of infrared and visible radiances for ISCCP, J. Climate, 6, 2341–2369, https://doi.org/10.1175/1520-0442(1993)006<2341:CDUSMO>2.0.CO;2. 1993.

Rossow, W. B. and Schiffer, R. A.: Advances in understanding clouds from ISCCP, Bull. Amer. Meteor. Soc., 80, 2261–2288, https://doi.org/10.1175/1520-0477(1999)080<2261:AIUCFI>2.0.CO;2, 1999.

~~.: Storm morphology and rainfall characteristics of TRMM precipitation features, Mon. Weather Rev., 134, 2702~~ 2721, ~~https://doi.org/10.1175/mwr3200.1, 2006.~~

Sauvageot, H., Mesnard, F., and Tenório, R. S.: The relation between the area-average rain rate and the rain cell size distribution parameters, J. Atmos. Sci., 56, 57–70, https://doi.org/10.1175/1520-0469(1999)056<0057:TRBTAA>2.0.Co;2, 1999.

Schumacher, C. and Houze, R. A.: The TRMM precipitation radar's view of shallow, isolated rain, J. Appl. Meteorol., 42, 1519–1524, https://doi.org/10.1175/1520-0450(2003)042<1519:TTPRVO>2.0.CO;2, 2003.

Simpson, J., Kummerow, C., Tao, W.-K., and Adler, R. F.: On the Tropical Rainfall Measuring Mission (TRMM), Meteorol. Atmos. Phys., 60, 19–36, https://doi.org/10.1007/BF01029783,1996.

Sun, L. L. and Fu, Y. F.: A new merged dataset for analyzing clouds, precipitation and atmospheric parameters based on ERA5 reanalysis data and the measurements of the Tropical Rainfall Measuring Mission (TRMM) precipitation radar and visible and infrared scanner, Earth Syst. Sci. Data, 13, 2293–2306, https://doi.org/10.5194/essd-13-2293-2021, 2021.

Viltard, N., Kummerow, C., Olson, W. S., and Hong, Y.: Combined use of the radar and radiometer of TRMM to estimate the influence of drop size distribution on rain retrievals, J. Appl. Meteorol., 39, 2103–2114, https://doi.org/10.1175/1520-0450(2001)040<2103:Cuotra>2.0.Co;2, 2000.

Wang, Y., Fu, Y. F., Liu, G. S., Liu, Q., and Sun, L.: A new water vapor algorithm for TRMM Microwave Imager (TMI) measurements based on a log linear relationship, J. Geophys. Res., 114, D21304, https://doi.org/10.1029/2008JD011057, 2009.

Wu, Z. H. and Fu, Y. F.: A new dataset of rain cell generated from observations of the Tropical Rainfall Measuring Mission (TRMM) precipitation radar and visible and infrared scanner and microwave imager

设置了格式: 字体: 10 磅
设置了格式: 字体: 10 磅
设置了格式: 字体: 10 磅
带格式的: 行距: 1.5 倍行距
设置了格式: 字体: 10 磅
设置了格式: 字体: 10 磅
设置了格式: 字体: Times New Roman, 10 磅
设置了格式: 字体: 10 磅
设置了格式: 字体: 10 磅
设置了格式: 字体: 10 磅
设置了格式: 字体: 10 磅
设置了格式: 字体: 10 磅
带格式的: 行距: 1.5 倍行距

[~~dataset~~], ~~Zenodo, https://doi.org/10.5281/zenodo.8352587, 2023~~Data set], Zenodo, https://doi.org/10.5281/zenodo.13118878, 2024.

Yokoyama, C., Zipser, E. J., and Liu, C.: TRMM-Observed shallow versus deep convection in the eastern pacific related to large-scale circulations in reanalysis datasets, J. Climate, 27, 5575–5592, https://doi.org/10.1175/JCLI-D-13-00315.1, 2014.

Yuter, S. E. and Houze, R. A.: Three-Dimensional kinematic and microphysical evolution of florida cumulonimbus. Part II: frequency distributions of vertical velocity, reflectivity, and differential reflectivity, Mon. Weather ~~Review~~Rev., 123, 1941–1963, https://doi.org/10.1175/1520-0493(1995)123<1941:Tdkame>2.0.Co;2, 1995.

~~Zhang, A. Q., Chen, C., Chen~~Zhou, Y. ~~L., Li~~., Lau, W. ~~B. A., Chen, S.~~K., M., and ~~Fu, Y. F.: Resilient dataset~~Liu, C. T.: Rain characteristics and large-scale environments of ~~rain clusters~~precipitation objects with ~~life cycle evolution during April to June 2016 2020 over eastern Asia based on~~extreme rain volumes from TRMM observations ~~from the GPM DPR and Himawari-8 AHI, Earth Syst. Sci. Data, 14, 1433–1445~~, J. Geophys. Res.-Atmos., 118, 9673–9689, https://doi.org/10.~~5194/essd-14-1433-2022, 2022~~1002/jgrd.50776, 2013.

Zipser, E. J. and Lutz, K. R.: The vertical profile of radar reflectivity of convective cells: A strong indicator of storm intensity and lightning probability?, Mon. Weather Rev., 122, 1751–1759, https://doi.org/10.1175/1520-0493(1994)122<1751:Tvporr>2.0.Co;2, 1994.

设置了格式: 字体: 10 磅
设置了格式: 字体: 10 磅
设置了格式: 字体: 10 磅
带格式的: 行距: 1.5 倍行距
设置了格式: 字体: 10 磅
设置了格式: 字体: 10 磅
设置了格式: 字体: 10 磅
设置了格式: 字体: 10 磅
设置了格式: 字体: 10 磅
设置了格式: 字体: 10 磅
设置了格式: 字体: 10 磅
设置了格式: 字体: 10 磅
设置了格式: 字体: 10 磅